

Rational Synthesis and Regulation of Hollow Structural Materials for Electrocatalytic Nitrogen Reduction Reaction

Cong Xue, Xinru Zhou, Xiaohan Li, Nan Yang, Xue Xin, Yusheng Wang, Weina Zhang, Jiansheng Wu, Wenjing Liu,* and Fengwei Huo*

The electrocatalytic nitrogen reduction reaction (NRR) is known as a promising mean of nitrogen fixation to mitigate the energy crisis and facilitate fertilizer production under mild circumstances. For electrocatalytic reactions, the design of efficient catalysts is conducive to reducing activation energy and accelerating lethargic dynamics. Among them, hollow structural materials possess cavities in their structures, which can slack off the escape rate of N_2 and reaction intermediates, prolong the residence time of N_2 , enrich the reaction intermediates' concentration, and shorten electron transportation path, thereby further enhancing their NRR activity. Here, the basic synthetic strategies of hollow structural materials are introduced first. Then, the recent breakthroughs in hollow structural materials as NRR catalysts are reviewed from the perspective of intrinsic, mesoscopic, and microscopic regulations, aiming to discuss how structures affect and improve the catalytic performance. Finally, the future research directions of hollow structural materials as NRR catalysts are discussed. This review is expected to provide an outlook for optimizing hollow structural NRR catalysts.

nitrogen in the human body is currently derived from synthetic NH_3). However, the hydrogen as reagent in this method is mainly produced by steam reforming using natural gas or fossil fuels, and the reaction process is carried out at high temperature and high pressure, which consumes plenty of energy (about 1–2% of the total global energy consumption) and releases a large amount of CO_2 (about 1% of the global annual CO_2 emissions).^[5,6] Considering energy shortages and increasing environmental problems, it is urgent to develop an energy-saving, environmentally friendly, green, and sustainable method to replace the traditional Haber–Bosch method to fix nitrogen.

Various strategies on N_2 fixation under mild conditions have been developed in recent years, such as mimicking biological nitrogenase,^[7,8] photocatalytic nitrogen fixation,^[9,10] and electrocatalytic nitrogen fixation.^[11,12] Compared with the


traditional resource-intensive Haber–Bosch method, electrocatalytic nitrogen reduction reaction (NRR) shows great potential to realize small-scale, distributed, and even on-site direct synthesis of NH_3 by utilizing water as a hydrogen source and renewable energy such as wind, solar, and tidal energy as power sources. In this way, the synthesized NH_3 can be further converted to supply crops, thereby saving the cost of nitrogen during transportation and storage.^[13–15] In practice, the limitation of N_2 activation prompts us to find a suitable and efficient way to break its inert bonds. Concurrently, an inevitable issue is the competitive hydrogen evolution reaction (HER) in the aqueous electrolyte, which will cause the reducing the Faradaic efficiency (FE).^[14,16]

In order to improve catalytic activity and selectivity, the development of efficient catalysts is essential for electrocatalytic nitrogen fixation. Currently, researchers have made enormous efforts in designing catalysts, including noble metal catalysts, non-noble metal catalysts, and nonmetal catalysts.^[17–19] In addition, many effective strategies have been developed to regulate the physical and chemical properties of catalysts to enhance their catalytic activity. For example, the structure and morphology of these materials (2D flakes, porous structure, hollow structure, etc.) were optimized to increase the apparent activity,^[20,21] defects (doping, vacancy, amorphous, etc.) were created to improve the intrinsic activity,^[22,23] various synthetic strategies (in situ synthesis method, immersion reduction method,

1. Introduction

Ammonia (NH_3) is not only widely used in the manufacture of fertilizers, pharmaceuticals, and chemical industries,^[1,2] but also is considered as a promising energy carrier because of its high hydrogen content (17.8 wt%), easy liquefaction, and convenient transportation.^[3,4] For over a century, NH_3 production has relied heavily on the traditional Haber–Bosch method. This method is considered to be one of the most significant invention of the 20th century as it triggers the revolution of modern agriculture and provided food security for population growth (at least half of the

C. Xue, X. Zhou, X. Li, N. Yang, X. Xin, Y. Wang, W. Zhang, J. Wu, W. Liu, F. Huo
Key Laboratory of Flexible Electronics (KLOFE) and Institute of Advanced Materials (IAM)
Nanjing Tech University
30 South Puzhu Road, Nanjing 211816, China
E-mail: iamwjliu@njtech.edu.cn; iamfwhuo@njtech.edu.cn

 The ORCID identification number(s) for the author(s) of this article can be found under <https://doi.org/10.1002/advs.202104183>

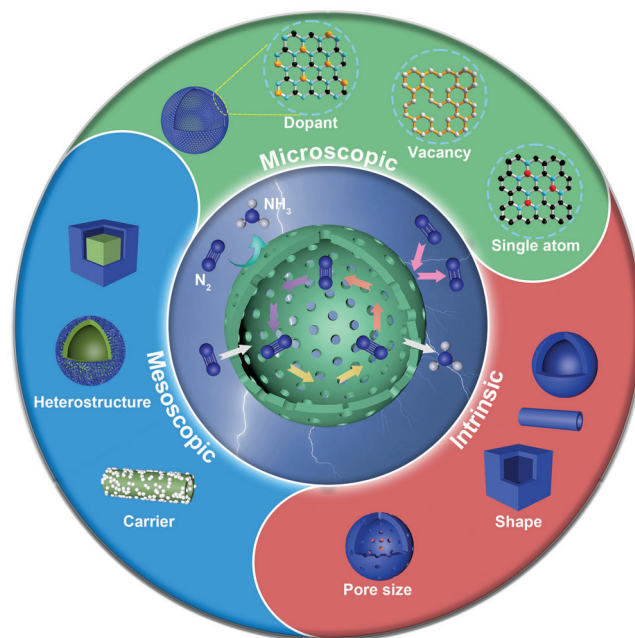
© 2021 The Authors. Advanced Science published by Wiley-VCH GmbH. This is an open access article under the terms of the Creative Commons Attribution License, which permits use, distribution and reproduction in any medium, provided the original work is properly cited.

DOI: 10.1002/advs.202104183

electrodeposition method, etc.) were adopted to obtain the catalysts grown on the electrode to reduce interface resistance,^[24,25] compounds were loaded with some other conductive materials (carbon black, graphene, carbon nanotubes, etc.) to promote charge transfer,^[26,27] etc.

Among them, hollow structural materials, a category of structures consisting of defined shell layers and internal cavity, have received extensive attention due to their unique structure and excellent performance according to the following advantages. First, considering the issue of weak solubility of N_2 in aqueous electrolytes, the hollow structural materials can give full play to their structural merits. The hollow structural cavity can be used as a nanoreactor to restrict the reactants, prolong the residence time of N_2 , increase the collision probability of N_2 , and improve the contact between N_2 and active sites, thereby expediting the reaction rate.^[28] Meanwhile, this restriction increases the concentration of local reaction intermediates in the cavities to accelerate further reactions and improve the NRR reaction kinetics.^[29,30] Second, sufficient exposure of active sites is key to efficiently catalyzing the conversion of N_2 to NH_3 . No matter it is the capping agents used in the synthesis of the catalysts, or the polymer binders (Nafion) required to support the catalysts on the reactive electrode, the exposure of active sites is inevitably affected.^[31] However, the cavities in the hollow structural materials are less affected by these factors and can better expose the active sites. Third, the N_2 diffusion velocity is also a key step of NRR. The tightly connected cavities of the hollow structural materials and the gaps between different structures have high permeability, which can provide a fast diffusion channel for N_2 .^[32] Last but not the least, catalytic durability is an important indicator for evaluating the performance of catalysts. The self-supporting 3D structure of the hollow material has excellent structural stability and helps to obtain good catalytic durability.^[33,34] In addition, various strategies have been developed to optimize the apparent activity and intrinsic activity of hollow structural materials to further improve their catalytic performance. In short, hollow structural materials have attracted much attention as excellent catalyst candidates and have been widely used in electrocatalytic reactions.

This review focuses on the latest development of hollow structural materials for nitrogen reduction reaction under environmental conditions. First, the reaction mechanisms of NRR will be introduced. Second, the common synthetic methods of hollow structural materials are summarized and divided into three categories: hard template method, soft template method, and self-template/template-free method. Then, a comprehensive introduction of NRR catalysts according to the sizes and types of catalysts is summarized from the following three aspects: 1) intrinsic regulation of hollow structural catalysts, focusing on the influence of shape and pore size of the hollow structural materials on the catalytic performance; 2) mesoscopic regulation of hollow structural catalysts, focusing on the combination of hollow structural materials and other molecular ingredients on NRR catalytic performance; 3) microscopic regulation of hollow structural catalysts, focusing on the influence of dopant, vacancy, and single-atom regulation on the active site modification of the hollow structural catalysts (Scheme 1). Finally, challenges and possible solutions faced by hollow structural materials as NRR electrocatalysts will be proposed. It is anticipated that this review will



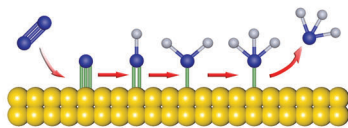
Scheme 1. Schematic diagram of hollow structural catalysts for NRR. Hollow structural materials according to the regulation strategy toward NRR are divided into three main sections: 1) intrinsic regulation (shape, pore size); 2) mesoscopic regulation (loading nanomaterials, construction of heterostructures); 3) microscopic regulation (doping engineering, vacancy engineering, single atom engineering, etc.).

provide valuable insights into the synthesis and design of the next-generation efficient hollow structural NRR catalysts.

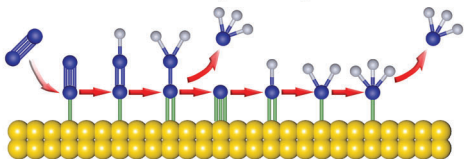
2. Reaction Mechanisms of NRR

In general, NRR occurs in three steps: i) adsorption of N_2 on active sites, ii) hydrogenation of the adsorbed N_2 , iii) NH_3 desorption. Specifically, according to the different sequence of $N\equiv N$ cleavage and hydrogenation, two possible mechanisms have been proposed: i) dissociative pathway, ii) associative pathway.^[35] As shown in Figure 1a, in the dissociative pathway, $N\equiv N$ cleavage occurs before hydrogenation. The $N\equiv N$ triple bond in nitrogen is dissociated first, and then the cracked N adsorbs on the catalyst surface and hydrogenates inch by inch until NH_3 is generated and released. Since extremely high energy is required for breaking $N\equiv N$, the dissociative pathway is mainly found in the Haber–Bosch process of industrial nitrogen fixation with high energy consumption. For associative pathway, $N\equiv N$ cleavage occurs in the hydrogenation process and can be divided into i) associative distal pathway and ii) associative alternating pathway according to the different hydrogenation sequences of two N atoms. As shown in Figure 1b, in the associative distal pathway, one end of the N_2 molecule is adsorbed on the catalyst surface, and the N atom far away from the catalyst surface is hydrogenated first until NH_3 is generated and released. Subsequently, the remaining N atom undergoes the same procedure and is released. Differently, in the associative alternating pathway (Figure 1c), the hydrogen atoms alternately combine with two N atoms until NH_3

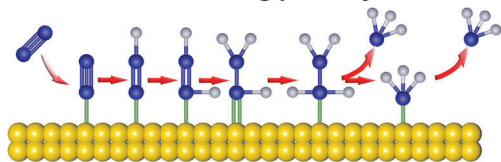
a. Dissociative pathway



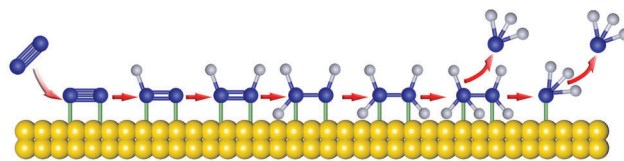
b. Associative distal pathway



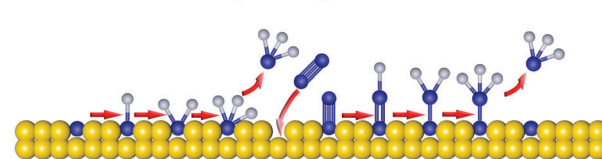
c. Associative alternating pathway



d. Enzymatic pathway



e. Mars-van Krevelen pathway



f. Surface-hydrogenation pathway

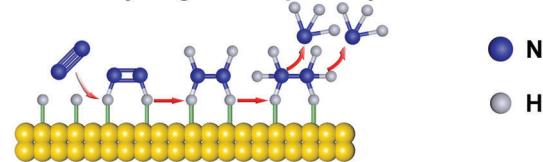


Figure 1. a–f) Schematic diagram of possible reaction mechanisms for NRR on the catalyst surface. The blue balls represent nitrogen atoms, and the gray balls represent hydrogen atoms.

is released, despite that one end of the N_2 molecule is adsorbed on the surface of the catalyst just like that in the associative distal pathway. In addition to the abovementioned cases where only one N atom in the N_2 molecule is adsorbed on the surface of the catalyst, an enzymatic pathway has been proposed in which two N atoms of the N_2 molecule are adsorbed on the surface of the catalyst simultaneously.^[36] As shown in Figure 1d, in the enzymatic pathway, the two N atoms adsorbed on the surface of the catalyst are hydrogenated sequentially, and finally NH_3 is generated and released.

Furthermore, a new mechanism Mars–van Krevelen (MvK) pathway that occurs on transition metal nitrides has been proposed by Abghoui and Skúlason and verified by theoretical calculations.^[37–40] The adsorption of N_2 molecules on the catalyst surface needs to undergo endothermic process and the N_2 dissociation also needs to overcome a very strong barrier, making the dissociative pathway difficult to occur. The hydrogenation of $*N_2$ to $*N_2H$ requires a large bias voltage, which is not favorable for the associative pathway. Although the associative–dissociative mixed pathway may also occur, MvK on transition metal nitrides occurs most favorably because the MvK pathway on metal nitrides has the lowest overpotential. In the MvK pathway, unlike the conventional one, hydrogenation first takes place on the lattice nitrogen on the surface of the transition metal nitrides until NH_3 is formed and released. Subsequently, the resulting nitrogen vacancies chemically adsorb N_2 molecules and follow the associative distal pathway for hydrogenation (Figure 1e).

Although many studies have shown that N_2 molecules can achieve the electrochemical conversion from N_2 to NH_3 at very low potential on noble metals. However, none of the existing NRR reaction pathways are suitable for these catalysts, whether dissociative pathway or associative pathway. Wang and co-workers discovered a novel NRR mechanism called surface-hydrogenation mechanism through first principle calculations.^[41] Unlike the

traditional reaction pathway, H^+ reduction occurs first on the noble metal catalyst surface instead of N_2 adsorption. It is proposed to explain the differences between experimental and computational methods. First, H^+ is reduced to $*H$, which is the potential determining step (PDS). Second, N_2 is activated and reduced to $*H_2N_2$, which is considered as a rate-determining step. Subsequently, $*H_2N_2$ is further reduced to NH_3 and released (Figure 1f). Moreover, proton supply is particularly critical for the catalytic activity of NRR during proton-coupled electron transfer (PCET) reaction. Some studies have shown that pH values can affect proton supply, leading to selectivity differences.^[42,43] In addition to pH values, Yin and co-workers found that some alkali metal cations (Li^+ , Na^+ , K^+ , and Cs^+) can regulate the proton transfer rate to inhibit HER and increase catalyst selectivity.^[44] It can be seen that although theoretical calculation has become a powerful means to judge the reaction mechanism, it is generally based on idealized models, inevitably ignoring many factors, so it is essential to combine theory with experiment. At the same time, there is an urgent need to develop and apply in situ test and characterization methods to accurately define the reaction process.

3. Synthetic Methods for Hollow Structural Materials

In the electrocatalysis field, the unique architecture of hollow materials endows them with potential catalytic possibilities. For example, the well-defined cavity could slack off the escape rate of N_2 and reaction intermediates, the high surface area could provide abundant exposure of active sites, the low density reduces the mass and charge transfer diffusion length. Therefore, the catalytic activity of hollow materials is generally affected by their structure and composition. In order to obtain better catalytic performance, it is necessary to carefully design hollow structural materials. Hence, it is critical to understand and choose the

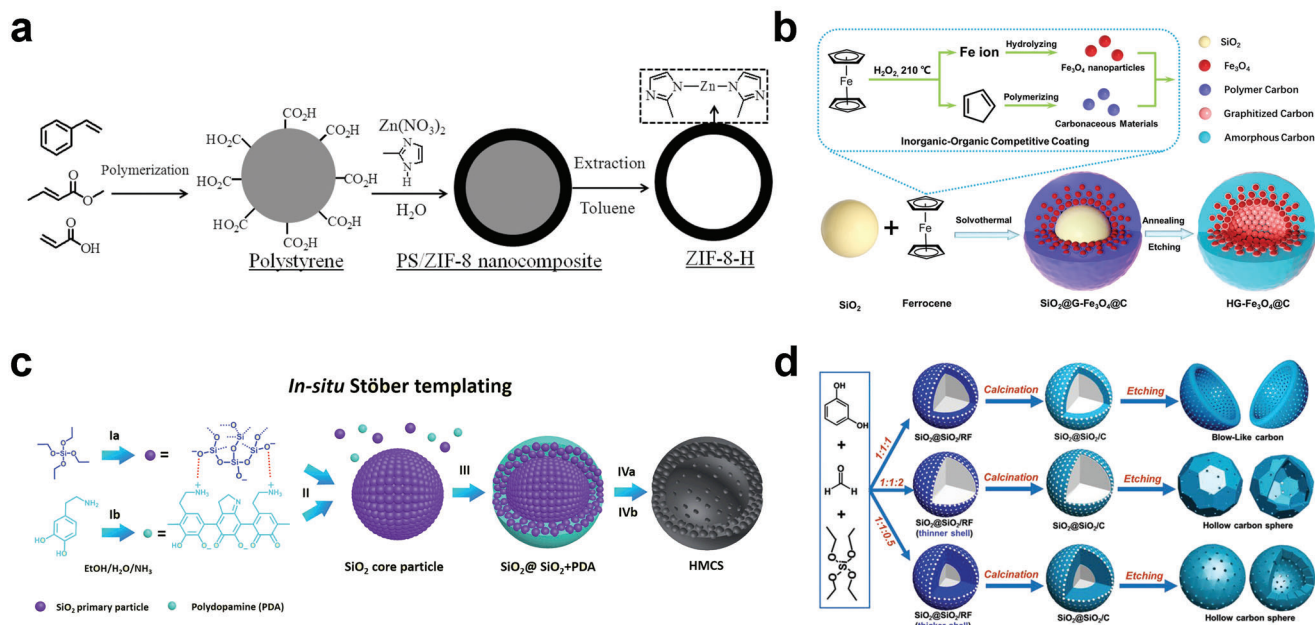


Figure 2. Synthesis of hollow structural materials via hard template method. a) Schematic diagram of fabrication of ZIF-8-H. Reproduced with permission.^[45] Copyright 2014, American Chemical Society. b) Schematic illustration for the synthesis of the hollow gradient structured Fe₃O₄@C nanospheres by an inorganic–organic competitive coating strategy. Reproduced with permission.^[46] Copyright 2021, Springer Nature. c) Schematic diagram of the in situ Stober templating of HMCS. Reproduced with permission.^[52] Copyright 2016, Royal Society of Chemistry. d) Scheme of the synthetic process of HBC or hollow carbon sphere (HCS) with different shell thicknesses via adjusting mass ratio of reagents. Reproduced with permission.^[53] Copyright 2020, Wiley-VCH.

appropriate method for controllable synthesis. This section will summarize the synthetic methods of hollow structural materials from three categories: hard template method, soft template method, and self-template/template-free method to better understand the synthetic methods of hollow structural materials and characteristics of variform approaches.

3.1. Hard Template Method

The hard template method, as the name suggests, uses rigid material as the template to be covered with the prepared material in the outer layer. Then, the desired hollow structural materials are obtained by removing the template. Generally speaking, the shapes of the hollow structural materials ultimately depend on the shape of the template. The parameters of hollow structural materials, such as the size, shell thickness, shell number, and pore size, can be controlled by adjusting the raw material concentration, pH values, reaction temperature, reaction time, and other conditions. It is worth noting that materials with poor chemical stability and high temperature instability are difficult to be developed by hard template method because the removal of the template inevitably requires the use of etching or high temperature calcination. After more than 20 years of development, the kinds of common hard template materials are enriched, including polystyrene (PS) balls, silica, carbon balls, metal particles, etc.

Li and co-workers developed a hollow zeolitic imidazolate framework-8 nanosphere (ZIF-8-H) based on the hard template method.^[45] First, carboxylate-terminated PS nanospheres were synthesized as hard templates, and then ZIF-8 was grown on

the surface of the spheres through the coordination of COOH functional groups with Zn ions and 2-methylimidazole. Finally, toluene was used to remove the PS template to obtain ZIF-8-H (Figure 2a). Recently, Zhao and co-workers prepared Fe₃O₄@C nanospheres with a hollow gradient structure (HG-Fe₃O₄@C) through an organic–inorganic competitive coating strategy by using SiO₂ as the hard template.^[46] In their strategy, ferrocene could be hydrolyzed in solvent to form Fe₃O₄, and it could also be polymerized to form carbon. The formed Fe₃O₄ and carbon would compete with each other and be deposited on the surface of SiO₂ to obtain SiO₂@G-Fe₃O₄@C. Then, the as-synthesized materials were treated by high temperature and etching to remove SiO₂ to obtain HG-Fe₃O₄@C (Figure 2b). In addition to hollow nanosphere, for example, nanofibers,^[47,48] nanotube arrays,^[49,50] and nanocubes,^[51] were successfully achieved by utilizing SiO₂, metal oxides, anodic aluminum oxide, and zeolite as the hard templates.

However, it is necessary to synthesize the hard template first, and then coat the required materials on the surface of the template in the abovementioned methods. Considering the cost and the simplification of experimental procedures, some in situ synthetic methods which integrate the template creation with the coating materials as one step have been developed to obtain materials in a convenient way. Yu and co-workers developed an in situ Stober template method to prepare hollow mesoporous carbon spheres (HMCSs).^[52] First, tetraethyl orthosilicate (TEOS) was hydrolyzed and condensed into 2–3 nm SiO₂ nanoparticles, and then monodispersed SiO₂ clusters were formed by secondary nucleation (Figure 2c). Subsequently, polydopamine (PDA) oligomers were polymerized by coating dopamine and

SiO₂ nanoparticles were cocondensed to SiO₂ clusters to form a SiO₂@SiO₂/PDA core-shell structure, and then HMCS was obtained by carbonization and NaOH etching. This in situ synthetic method avoids the introduction of surfactants and is therefore more economical. Meanwhile, the pore size and shell thickness of HMCS can be easily adjusted by changing the ratio of reagents and the growth time of SiO₂ and PDA. Very recently, Fan and co-workers developed hollow bowl carbon (HBC) structures using similar in situ SiO₂ template methods (Figure 2d).^[53] They found that alteration in the ratio of resorcinol (R), formaldehyde (F), and TEOS would determine the final morphology of the materials, in the case where the ratio of the above three compounds was 1:1:1, HBC was successfully formed due to effect of capillary after removing SiO₂ by hydrofluoric acid etching.

In addition to simple single-shell hollow structural materials, many complex hollow materials with multishelled structures can also be prepared by the hard template method. For example, Yeh and co-workers synthesized double-shelled and triple-shelled mesoporous SiO₂ nanospheres via the shell-by-shell method.^[54] They coated SiO₂ layer by layer on the PS sphere template, and further employed protective etching to prepare nanospheres with different shell layers (Figure 3a). The study found that the introduction of 3-aminopropyltriethoxysilane is extremely important for the protection of the second layer of SiO₂, and the introduction of polyvinylpyrrolidone (PVP) playing passivation effect on the second and third layers of SiO₂ is also key to form multishelled compounds. Although the shell-by-shell method is relatively simple in design, and multiple-shelled layers can also be prepared by repeated steps, the cumbersome steps in practical operation hinder its large-scale promotion and application. Furthermore, choosing a suitable template to ensure uniform coating of the material also affects the general applicability of the method. To solve these problems, Wang and co-workers developed a one-step synthetic method using carbon microspheres (CMSs) as hard templates to prepare multishelled hollow metal oxide microspheres. They prepared a series of spinel ferrites (MFe₂O₄, M = Zn, Co, Ni, Cd) using CMSs as sacrificial templates for the first time.^[55] In 2011, this method was officially named as the sequential template method (Figure 3b).^[56] Specifically, metals ions adsorbed on the surface of CMS template were first accumulated and oxidized until the formation of metal oxide shell by pyrolysis process. As the combustion progressed, the CMS was separated from the metal oxide shell due to the volume of the CMS template being decreased. Subsequently, the remaining CMS could further act as a template and the above process was repeated to form inner shell layers. Different from the traditional hard template method, CMS was used as a carrier for adsorbing metal ions and a continuous template to construct a multishell hollow structure in the sequential template method. In short, this simple and convenient method is very conducive to large-scale production.

Furthermore, various parameters of multishelled hollow structural materials, such as the shell layer numbers, shell thicknesses, shell spacing, and shell sizes, can be better controlled by adjusting various conditions during the adsorption and heat treatment processes. In the process of adsorbing metal ions, adsorption time, metal ion concentration, adsorption temperature, solvent type, and pH values are all adjustable variables. During heat treatment, the selection of atmosphere, heating rate, and du-

ration time are particularly important. For example, Wang and co-workers systematically studied the effects of adsorption temperature and time, precursor concentration, solvent composition, heat treatment atmosphere, and other conditions on materials (Figure 3c).^[57] Another example is that hollow Mn₂O₃ microspheres with different numbers of shell layers were prepared, as the pH values increased, the shell layer numbers increased (Figure 3d).^[58] This is due to the increase in the negative charge on the surface of CMSs as the pH values increases, so that more positively charged Mn ions can be attracted through electrostatic attraction. Finally, under the same conditions, expect the changing pH values; single-shelled, double-shelled, and triple-shelled hollow Mn₂O₃ microspheres were obtained at pH values of 3.35, 4.43, and 6.43, respectively. Besides, the shell layer numbers can also be adjusted by controlling the rate of crystallization. For example, the crystallization rate can be adjusted by changing the molar ratios of the reagents to obtain hollow microspheres with different shell layers (Figure 3e).^[59] Furthermore, the heating rate will affect the speed of template removal and shell spacing. For instance, triple-shelled ZnO microspheres with different shell spacings were prepared by changing the heating rates (Figure 3f).^[60] Apart from CMSs, metal-organic frameworks (MOFs),^[61,62] polymers,^[63,64] metal carbonates^[65] can also be used as templates to synthesize hollow multishelled materials by the sequential template method.

3.2. Soft Template Method

In addition to materials used in hard template method, micelles/vesicles, emulsions, bubbles, etc., can also act as templates to prepare hollow nanostructures. This method is called soft template method, and is often related with less rigid materials. In contrast to the hard template method that demands hard conditions to remove the template, the soft counterpart only involves simple cleaning or extraction. Under certain circumstances, it is not even necessary to consider the removal of the template. Therefore, the preparation of hollow structural materials by the soft template method is a viable option for those chemically and thermally unstable materials. However, compared with the hard template method, the soft template method shows poorer control over the shape, shell thickness, and size of the hollow structural materials, which is urgently needed to be solved. So far, according to classification of soft templates, the soft template method can be divided into the following categories: 1) micelle/vesicle method, 2) emulsion method, 3) bubble method, and 4) spray method.

Micelles/vesicles are formed by self-assembly of amphiphilic molecules with both hydrophilicity and lipophilicity in a single-phase solvent.^[66,67] Common amphiphilic molecules are block copolymers and surfactants. The micelles usually have a single-layer structure with the hydrophilic side facing outward, and the vesicles usually have a double-layered structure or a multilayer structure with only the hydrophilic side facing outward. The morphology and structure of the micelle/vesicle template can be changed by adjusting the pH values, temperature, concentration of amphiphilic molecules, and the ionic strength of the solution.^[68] After depositing the targeted material on the hydrophilic or hydrophobic interface of the micelle/vesicle, the hollow structural materials are formed by removing the template.

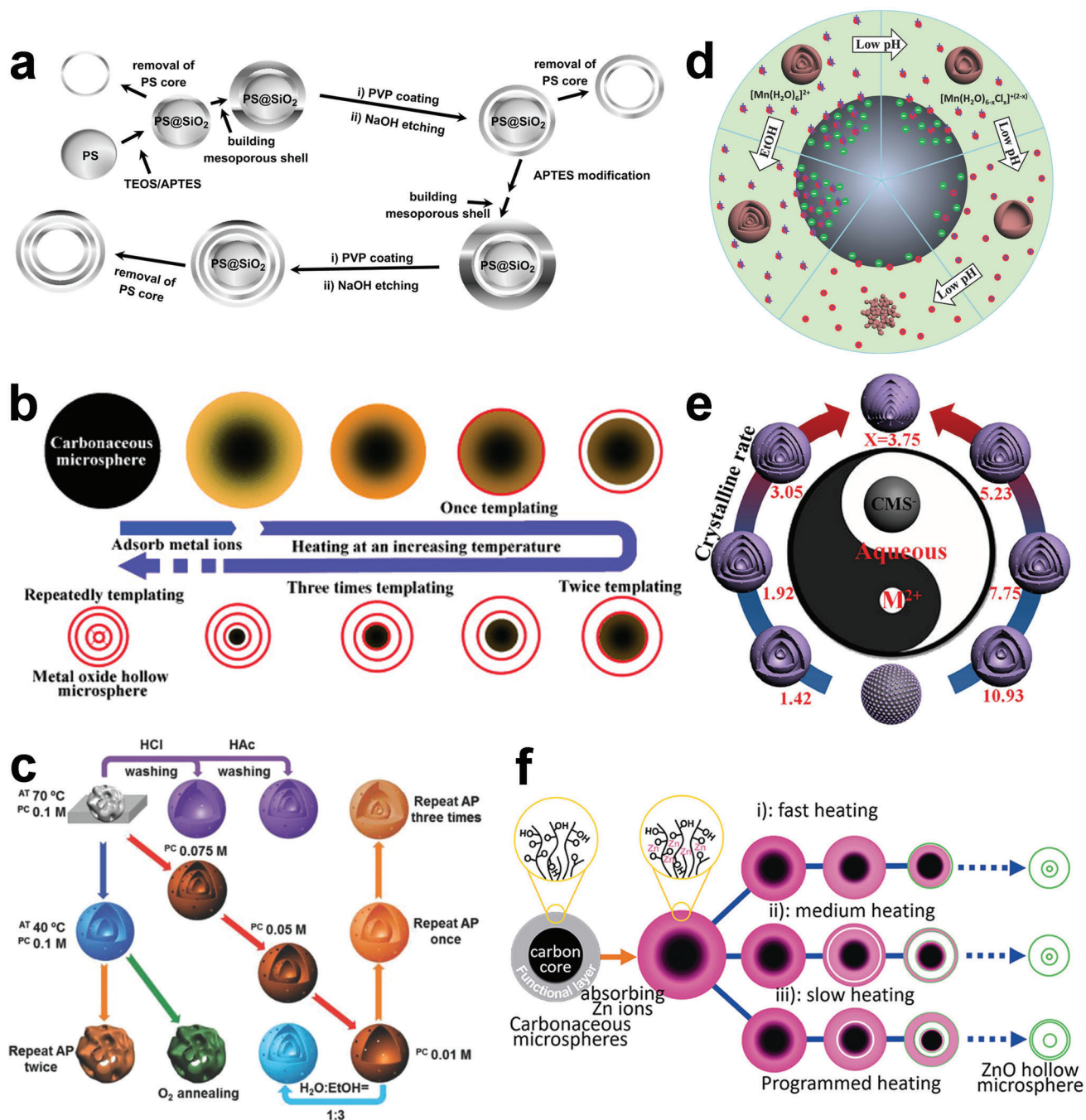


Figure 3. Synthesis of multishelled hollow structural materials via hard template method. a) Schematic diagram of the fabrication of hollow multishelled silica nanospheres. Reproduced with permission.^[54] Copyright 2011, Elsevier. b) Schematic diagram of the sequential template approach for the synthesis of multiple-shelled hollow metal oxide microsphere. Reproduced with permission.^[56] Copyright 2011, Wiley-VCH. c) Effects of synthetic conditions on the morphology of products. Reproduced with permission.^[57] Copyright 2016, Springer Nature. d) Scheme of synthetic mechanism for multishelled hollow microspheres and Mn₂O₃ nanoparticles under different adsorption conditions. Reproduced under the terms of the Creative Commons CC-BY license.^[58] Copyright 2014, The Authors. Published by Wiley-VCH. e) Control of the shell number of hollow microspheres by tuning the molar ratio of reagents. Reproduced with permission.^[59] Copyright 2017, Wiley-VCH. f) Schematic diagram of the generation of multishelled ZnO hollow microspheres via different heating processes. Reproduced with permission.^[60] Copyright 2012, Wiley-VCH.

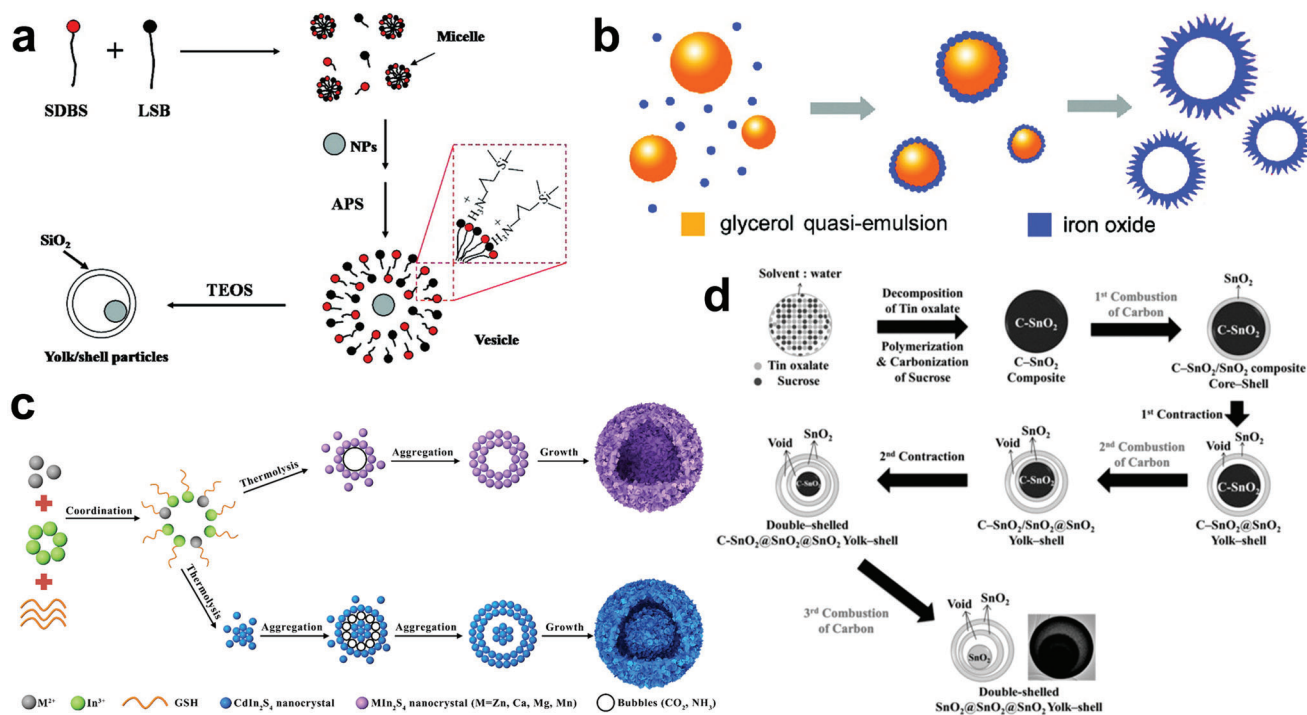


Figure 4. Synthesis of hollow structural materials via soft template method. a) Schematic diagram of the formation yolk/SiO₂ shell containing movable nanoparticles cores. Reproduced with permission.^[69] Copyright 2009, American Chemical Society. b) Mechanism of the generation of α -Fe₂O₃ hierarchical hollow spheres. Reproduced with permission.^[71] Copyright 2011, American Chemical Society. c) Schematic illustration of the ternary sulfide hollow and yolk-shell structure formation. Reproduced with permission.^[80] Copyright 2018, American Chemical Society. d) Scheme of the formation of the SnO₂ yolk-shell structure with different shell layers. Reproduced with permission.^[83] Copyright 2013, Wiley-VCH.

For example, Wu and Xu reported the strategy of synthesizing yolk-shell structure by soft template method first, and then used SiO₂ nanoparticles to encapsulate the yolk/shell particles (Figure 4a).^[69] In this work, lauryl sulfonate betaine and sodium dodecyl benzenesulfonate as mixed surfactants and templates were added to the solution forming micelle as nuclear precursor first. After that, 3-amino-propyltriethoxysilane (APS) as initiator was added to induce vesicle formation. It is worth noting that the partially protonated APS playing the role of directing agent was electrostatically adsorbed on the vesicles' surface. Then, TEOS was added to the vesicle and interacted with the terminal functional groups of APS by means of hydrolysis and condensation to form yolk/shell particles with SiO₂-encapsulated vesicles. In addition, this excellent template method can also be extended to encapsulate other nanoparticles, such as Au nanoparticles and spindle-shaped Fe₂O₃ particles.

Emulsion method usually refers to two or more immiscible liquids forming an emulsion with the aid of amphiphilic molecules. It has the characteristics of good particle dispersion and thermodynamic stability. The emulsion can be divided into water-based emulsion/oil-in-water and oil-based emulsion/water-in-oil according to the dispersion phase.^[70–73] The hollow structural materials can be prepared by depositing the targeted materials on the surface of the emulsion, and then removing the emulsion template by simple washing or calcination. Lou and co-workers reported the synthesis of α -Fe₂O₃ hollow nanospheres using quasiemulsion as a soft template (Figure 4b).^[71] In their strategy, glycerol was mixed with water to form a quasiemulsion,

which was partially polymerized to form an emulsified sphere under hydrothermal conditions, and then the adjunction of Fe precursor was hydrolyzed and aggregated on the surface of the emulsion template. The glycerin quasiemulsion can be simply removed by solvent extraction in the subsequent cleaning process.

The template removal requires reasonable design because improper strategies may not only make it difficult to completely remove the template, but also may bring out collapsing in the structure or the hole. In comparison, the bubble template method is a cost-effective and convenient method since there is no need to consider template removal. Currently, bubble template formation methods have been developed, including gas blowing method,^[74,75] chemical reaction method,^[76,77] and ultrasonic induction method.^[78,79] For example, Hu and co-workers synthesized a series of ternary sulfide hollow structural materials using the chemical reaction bubble template method (Figure 4c).^[80] Glutathione (GSH) as the source of bubble template could coordinate with metal ions M (such as Cd²⁺, Zn²⁺, Ca²⁺, Mg²⁺, and Mn²⁺) and In³⁺ through strong coordination to form complexes. MIn₂S₄ crystals were obtained through a further pyrolysis process, and driven by surface energy, the as-synthesized MIn₂S₄ crystals grew on the CO₂ and NH₃ bubbles which were released by pyrolysis, and finally ternary sulfide hollow structural materials were synthesized. It is worth noting that the coordination ability of metal ions and GSH is related to the ion radius of metal ions. When the metal ions are Cd²⁺ and In²⁺ with close ionic radius, their coordination ability with GSH will be weak, resulting in the formation of small-sized CdIn₂S₄

single crystals. The assembly speed of the sphere CdIn_2S_4 was the fastest because the smaller the single crystal size, the higher the surface energy, and the time of bubble formation would lag behind the assembly of these small-sized single crystals, leading to the production of yolk-shell structure.

The spray method is considered to be a soft template method with industrial application prospects, because it can continuously produce hollow structural materials on a large scale.^[81] The spray method can also be regarded as a special sequential template method, except that it does not require the synthesis of carbon microspheres in the first place. The general process of spray method is as follows: the mixed solution of metal salt and sucrose is atomized into droplets by the ultrasonic sprayer, and then the sucrose is polymerized and carbonized through a combustion process to compete with the crystallization of metal to form hollow structural materials.^[82] For instance, the SnO_2 yolk-shell structure was synthesized in a simple one-pot spray method by Kang and co-workers (Figure 4d).^[83] In their strategy, tin oxalate and sucrose were dissolved in water as precursors, the atomized droplets were formed under ultrasonic force, and the final carbon- SnO_2 particles were obtained through further pyrolysis and polymerization. They found that the pyrolyzation temperature of carbon and the concentration of oxygen would affect the morphology of the final product. At low temperature, the slow combustion of carbon and sufficient oxygen supply eventually facilitated the formation a single-shell $\text{SnO}_2 @ \text{SnO}_2$ with yolk-shell structure. On the contrary, under high temperature, the combustion of carbon only occurred on the surface, while the insufficient internal oxygen supply caused the internal C- SnO_2 core to shrink first, forming a C- $\text{SnO}_2 @ \text{SnO}_2$ yolk-shell structure. Furthermore, the insufficient internal oxygen supply led the above steps to be repeated in the C- $\text{SnO}_2 @ \text{SnO}_2$ yolk-shell structure and produced the final double-shell $\text{SnO}_2 @ \text{SnO}_2 @ \text{SnO}_2$ yolk-shell structure.

In short, the soft template can be easily removed to better preserve the composition and morphology of the material, which has unique advantages. For example, for the emulsion method, the emulsion can be removed by extraction instead of calcination, which would be an excellent choice for materials with poor thermal stability. The bubble method is cost-effective without removing template. Nevertheless, the soft template method has insufficient control over the thickness, shape, and size uniformity of the material. Here, it is suggested that researchers should pay more attention to the development of regulatory means for materials while studying the soft template method.

3.3. Self-Template/Template-Free Method

Different from the inert template materials used in the traditional hard template and soft template methods, the self-template/template-free method assisting in the formation of the targeted hollow structural materials without introducing inert additional templates has been developed recently. In some cases, the template material will eventually be transformed into the targeted hollow structural material or part of the targeted hollow structural material, and thus this strategy can be considered template-free. It can not only avoid cumbersome steps but also save costs, promising its industrial application value. How-

ever, it should be pointed out that there is still great room for the self-template/template-free method to improve in tuning the desired shape, size, and shell thickness of the hollow structural material. According to different synthetic principles, the self-template/template-free method can be divided into Ostwald ripening, Kirkendall effect, surface protection etching, galvanic replacement, etc.

Ostwald ripening is a physical phenomenon in which small particles with high surface energy are dissolved in a solvent and then deposited on larger particles to reduce the surface energy. In 2004, Yang and Zeng used Ostwald ripening for the first time to prepare hollow structural materials and synthesize hollow titanium dioxide spheres under hydrothermal conditions.^[84] Since then, various hollow structural materials have been synthesized based on Ostwald ripening, such as SnO_2 , TiO_2 , CuO , NiS , MoSe_2 , and covalent organic frameworks (COFs).^[85-91] For example, Huang and co-workers prepared COF hollow spheres via a self-template method based on Ostwald ripening principle (Figure 5a).^[91] COF crystallites were first nucleated with the lowest surface energy and further assembled into large solid microspheres. After that, the surface of the crystalline microspheres gradually became smooth due to the existence of the unreacted functional groups. Eventually, the COF hollow spheres were formed through inside-out Ostwald ripening principle. In addition, due to the different locations of Ostwald ripening, complete hollow structure, symmetrical core-shell structure, and asymmetrical core-shell structure were also produced.

The Kirkendall effect originally refers to the formation of voids due to the different diffusion rates between the diffusion of two metals at high temperatures. Alivisatos and co-workers developed the nanoscale Kirkendall effect that can be used to synthesize hollow structural materials in 2004.^[92] The nanoscale Kirkendall effect describes what happens when the internal diffusion rate of solid materials is greater than the external diffusion rate of the entire materials, an internal cavity will be generated inside the structure. At present, through reasonable design, the Kirkendall effect has made great achievements in the field of hollow structural materials, such as NiO nanoparticles, Co_3O_4 nanotubes, and Fe_3O_4 nanoshells.^[93-95] In addition, Jin and co-workers proposed a theoretical model that combined the positive and reverse Kirkendall effects for the first time to synthesize single-metal Pd hollow nanocrystals.^[96] They found that inserting the X element with fast diffusion rate into the M nanocube could form a solid MX, and then extracting the X would produce a hollow M nanocrystal, and the process can be repeated (Figure 5b). As the number of cycles increased, the diameter (D) of the sphere increased, and the shell thickness (T) of the nanocage became thinner. On this basis, the theory was applied to experiment, phosphorus was inserted into Pd nanocube precursor through the positive process of Kirkendall effect. It was concluded that the insertion of P would disrupt the lattice and induce the transition from the Pd nanocube to the Pd-P nanosphere. The subsequent reverse Kirkendall effect process happened, during which the P was extracted by the driving force of the outward diffusion caused by the oxidation of P at high temperature. Finally, the transformation of solid nanospheres into hollow nanocages was realized.

Unlike the soft/hard template method that requires other targeted materials as the sacrificial template, selective etching utilizes itself as the sacrificial template, which is also considered

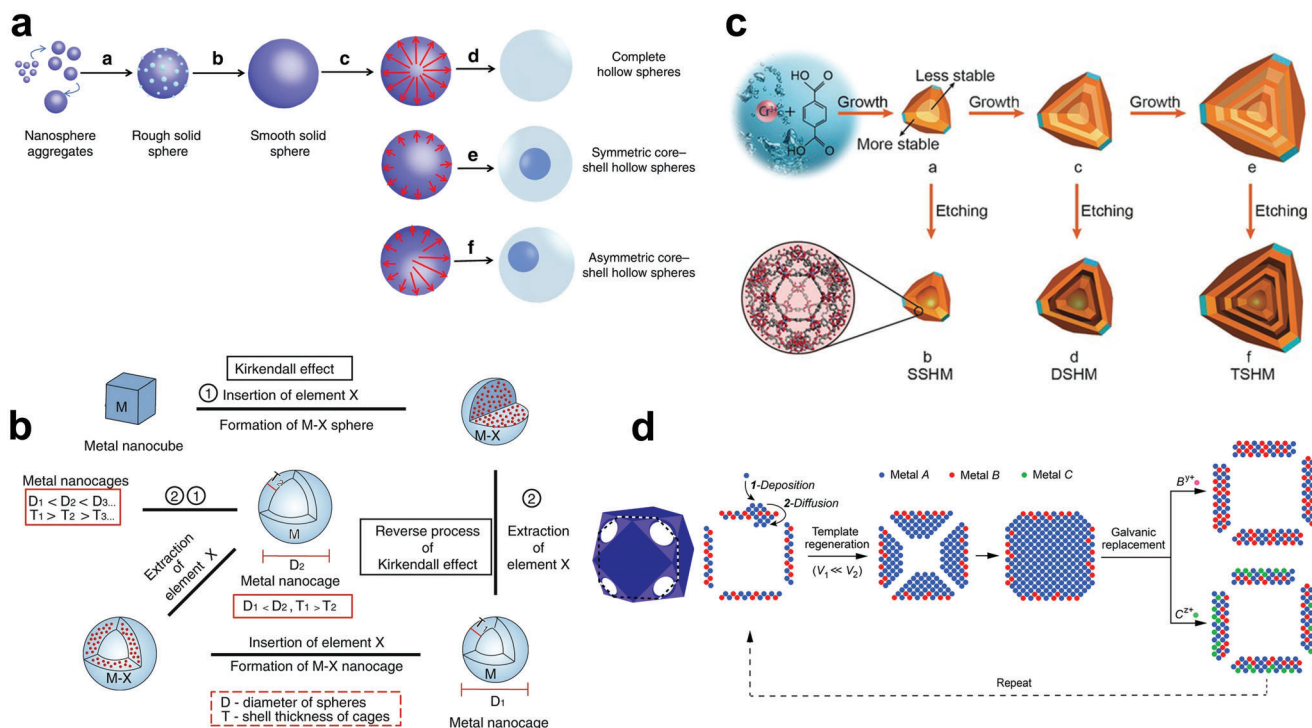


Figure 5. Synthesis of hollow structural materials via self-template/template-free method. a) Illustration of synthesis of COF hollow spheres by Ostwald ripening mechanism. Reproduced with permission.^[91] Copyright 2020, Springer Nature. b) Schematic diagram of the formation of hollow monometallic nanocrystals via repeated Kirkendall effect mechanism. Reproduced with permission.^[96] Copyright 2017, Springer Nature. c) Illustration of fabrication of hollow MIL-101 with different shell layers via selective etching mechanism. Reproduced with permission.^[104] Copyright 2017, Wiley-VCH. d) Schematic diagram of synthetic routes for highly diverse hollow nanostructures via template regeneration and galvanic replacement mechanism. Reproduced with permission.^[117] Copyright 2020, American Chemical Society.

to be an attractive self-template strategy for synthesizing hollow structural materials. Selective etching requires reasonable adjustment of materials to obtain available internal unevenness. The difference in solubility between the inner and outer regions of the initial material is considered to be the key to the formation of a hollow structure. Yin and co-workers first reported a selective etching method to prepare TiO₂ hollow microcapsules in 2007.^[97] They found that the addition of poly(acrylic acid) was the key to the formation of hollow structures. It can protect the surface of TiO₂ nanoparticles and slow down their removal in the subsequent etching process, thus effectively forming hollow structures. In the following year, they defined this method as “surface-protected etching” and synthesized hollow SiO₂ spheres, but introducing PVP as a surface-protecting agent to ensure the formation of the spheres.^[98] In addition to poly(acrylic acid) and PVP, polymers such as sodium dodecyl sulfate, polyethylene glycol, and polyethylene imine were also considered as effective surface-protecting agent for the construction of hollow structural materials. In addition, hollow structural materials such as Prussian Blue, Al₂O₃, ZnO, and CeO₂ can also be synthesized through this way.^[99–101]

Although surface-protected etching does not require a pre-synthesized template to save costs, the added surface-protecting agent becomes an additional cost burden. The researchers found that there is no surface-protecting agent when manufacturing the passivation layer, and hollow structural materials can also be synthesized by etching. This is due to the nonuniformity of

the self-template material itself caused by unevenly distributed defects.^[102–104] An intuitive example is that solid particles prepared by the liquid phase method possess a faster growth rate in the initial growth stage, which often results in the abundant defects in the core. For example, Huo and co-workers constructed multishelled hollow MOFs as catalysts for the first time through gradual crystal growth and subsequent selective etching (Figure 5c).^[104] The template of the selective etching method is itself, which serves not only as template, but also as the component of inner and outer shells, eliminating cumbersome heterogeneous coatings and making it more reproducible. However, it should be noted that it is important to avoid overetching and guarantee the accuracy of the etching.

Galvanic replacement is also an etching process, except that it requires electrode potential as the driving force. Typically, two metals with an electrochemical potential difference are selected as the anode and cathode. The metal A with a lower reduction potential is synthesized as the anode first, and then it is oxidized and dissolved when it is in electrical contact with cathode metal B with higher reduction potential. Meanwhile, metal B will be reduced and deposited on the outer surface of metal A. As the displacement reaction progresses, a hollow structural material with similar shape to metal A will eventually be constructed. In 2002, Xia and co-workers developed the Au–Ag hollow structural material for the first time using galvanic replacement.^[105,106] Inspired by this, various hollow structures were developed, such as nanotubes,^[107,108] nanorods,^[109,110] nanospheres,^[111,112]

nanocages,^[113,114] and nanoboxes.^[115,116] Very recently, Xia and co-workers reported a template regenerative galvanic replacement method that can be used to synthesize high-diversity hollow structural materials with highly adjustable parameters (Figure 5d).^[117] They first prepared a hollow A–B alloy nanocage by galvanic replacement, and then controlled the deposition rate to selectively grow metal A in the cavity of the hollow A–B alloy nanocage. Here, the inward diffusion rate of metal A was demanded to be much greater than the external diffusion rate to ensure that the atoms deposited on the outer surface could migrate into the cavity. The A@A–B nanostructures filled with the gaps were then used as templates for the next step of galvanic replacement. It is worth noting that this template regenerative galvanic replacement method can be repeated continuously when the nanocage has open voids, while metal A can also be replaced with alternated metal. Thus, this method breaks the stoichiometric limit of the original galvanic replacement to produce a hollow structural material with adjustable wall thickness and flexible composition.

The self-template/template-free method is a strategy for synthesizing hollow structural materials with simple synthetic steps, high repeatability, and large-scale production. Compared with hard template and soft template, the self-template/template-free method can produce nanoscale hollow structural material without considering heterogeneous coating. Here, the development of self-template/template-free method including Ostwald ripening, Kirkendall effect, selective etching, and galvanic replacement is briefly reviewed. In addition, there are many other efficient methods, such as solution regeneration,^[118,119] ion exchange,^[120,121] and self-assembly,^[122,123] which are not mentioned but also have referential value. As an emerging strategy, the advantages of using the self-template/template-free approach will be reflected in industrial applications in the future.

4. Hollow Structural Materials as NRR Catalysts

Hollow structural material is a kind of nanomaterial with inner cavity, and tubular hollow nanomaterial, spherical hollow nanomaterial, and cubic hollow nanomaterial are the most common ones. In recent years, hollow structural materials are considered to be excellent catalysts, which have been vigorously studied in the fields of photocatalysis and electrocatalysis due to their large specific surface area, low density ratio, rapid mass and charge transfer, and high structural stability.

As NRR catalysts, the hollow structural materials have the following advantages. 1) The internal surfaces of the hollow structural materials are less affected by the capping agents, which are more conducive to the catalysis. At the same time, the inner cavities can effectively capture N_2 and make N_2 constantly collide with the inner surface, thus increasing the opportunity for the reaction site to combine with N_2 . 2) The hollow structural materials have large specific surface area in both internal and external surfaces, and abundant channels can provide large contact areas for catalytic reaction, which are beneficial for exposing more active sites and shortening mass/charge transfer pathway to further enhance the performance of NRR. 3) The self-supported 3D geometries entitle the hollow structural catalysts with structural stability, which can effectively prevent the structural collapse during the catalytic process to obtain long-term catalytic stability. 4)

The highly unsaturated surface coordination makes the hollow structural materials have high loading capacity to disperse other active components and thus expose more N_2 adsorption sites. The above advantages encourage researchers to develop high-performance NRR catalysts based on hollow structural materials. In addition to hollow structural materials as intrinsic catalysts, diverse strategies have been developed by modifying and regulating the hollow structural materials in order to further enhance the catalytic activity. This section will summarize the development of hollow structural NRR catalysts from three main sections: 1) intrinsic regulation of hollow structural catalysts; 2) mesoscopic regulation of hollow structural catalysts; 3) microscopic regulation of hollow structural catalysts.

4.1. Intrinsic Regulation of Hollow Structural Catalysts

The hollow structural material is generally an open structure with porous shell, which helps maximize its structural advantages. Due to the existence of the cavity, the hollow material usually has large specific surface area, which would facilitate the catalytic reaction. When solid structural material is used as catalyst, the catalytic reaction only occurs on the outer surface, while when the hollow structural material acts as catalyst, the catalytic reaction occurs not only on the outer surface, but also in the pores and on the inner surface of the shell. In addition, the cavity can selectively transfer reactants, effectively limit N_2 and reaction intermediates, and increase their collisions in the cavity, so as to improve the catalytic reaction rate in the cavity. In a word, hollow structural materials as NRR catalysts have unique advantages. This section will introduce the progress of intrinsic regulation of hollow structural catalysts.

As we all know, the activity of catalysts is related to their structure. For hollow catalysts, the catalytic activity can be enhanced by adjusting their morphology, shell thickness, and pore size.^[124–127] According to the geometry, the hollow catalysts can be simply divided into spherical, tubular, and cubic structures. Among them, spherical hollow structural materials have been widely reported as NRR catalysts because their synthetic strategies are relatively simple. For example, Sun and co-workers have developed VO_2 hollow microspheres as NRR cathode materials.^[128] At -0.7 V versus reversible hydrogen electrode (RHE), a high NH_3 yield of $14.85 \mu g h^{-1} mg^{-1}_{cat.}$ and a FE of 3.97% were obtained efficiently and stably, which were twice that of solid VO_2 microspheres. In addition, they also synthesized hollow Bi_2MoO_6 spheres through a one-step hydrothermal reaction.^[129] Due to the excellent structure of the catalyst, it is possible to expose more active sites and the reaction intermediate can be easily diffused. At -0.6 V versus RHE, the FE and NH_3 yield reached 8.17% and $20.46 \mu g h^{-1} mg^{-1}_{cat.}$, respectively. Wang et al. reported a simple one-pot solvent method to prepare hollow and solid Bi nanospheres (Figure 6a).^[130] The specific surface area of hollow Bi nanospheres ($23.7 m^2 g^{-1}$) was nearly 16 times larger than that of solid Bi nanospheres (Figure 6b). Undoubtedly, such a high accessible surface area exposed more active sites. With the hollow Bi nanospheres as cathode materials, NRR was performed in N_2 -saturated $0.1 M Na_2SO_4$, and the highest NH_3 yield was $23.4 \pm 1.3 \mu g h^{-1} mg^{-1}_{cat.}$ at -0.4 V versus RHE, with the corresponding FE of $19.8 \pm 1.1\%$, which was over 2 times

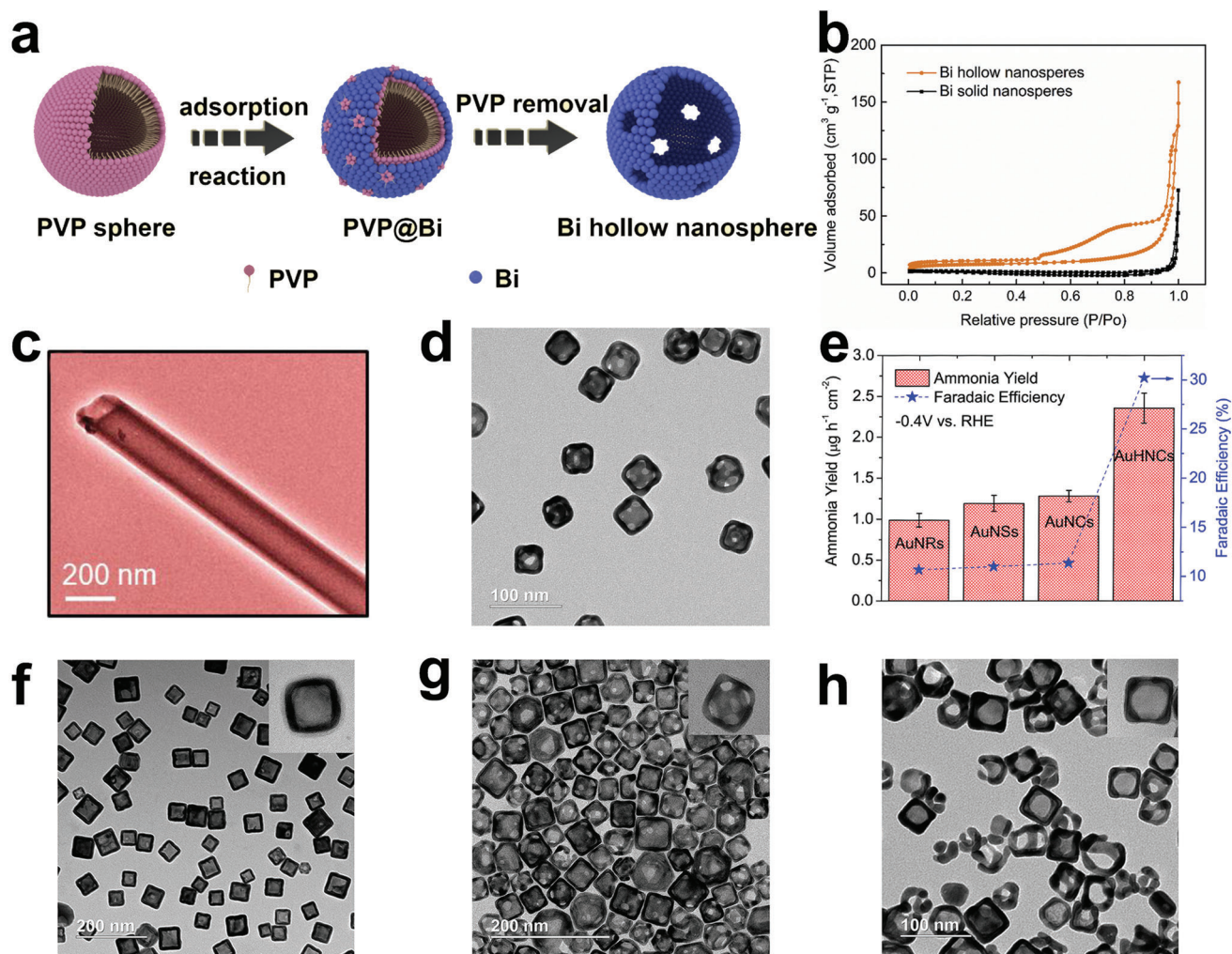


Figure 6. a) Schematic diagram of the synthesis of Bi hollow nanospheres. b) N_2 adsorption/desorption isotherms of different samples. Reproduced with permission.^[130] Copyright 2020, Elsevier. c) TEM image of CoPc NTs. Reproduced with permission.^[137] Copyright 2021, American Chemical Society. d) TEM image of AuHNCS. e) NH_3 yields and FEs of different catalysts. Reproduced with permission.^[31] Copyright 2018, Elsevier. f) TEM image of AuHNC-635. g) TEM image of AuHNC-715. h) TEM image of AuHNC-795. Reproduced with permission.^[138] Copyright 2018, American Chemical Society.

higher than the catalytic performance of solid Bi nanospheres. Sun and co-workers reported for the first time multishell hollow Cr_2O_3 microspheres as NRR catalysts with a maximum NH_3 yield of $25.3 \mu\text{g h}^{-1} \text{mg}^{-1} \text{cat.}$ and the corresponding FE was 6.78% at -0.9 V versus RHE.^[131]

Proton hydrogenation is also an important step in determining the reaction kinetics during the NRR reaction, especially for proton-deficient alkaline electrolytes. Previous studies have shown that the phosphate in metal phosphate can be used as a proton transport carrier to promote proton transfer to the active site.^[132] In addition, metal- N_2 battery, as a kind of dual-function secondary battery combining energy storage and artificial nitrogen fixation, has attracted extensive attention recently.^[133,134] In view of this, Yuan and co-workers derived hollow molybdenum phosphate microsphere (MoPi/HSNPC) by pyrolyzing molybdenum phosphate as a dual-function catalyst for Al- N_2 batteries.^[135] The MoPi/HSNPC achieved the highest NH_3 yield of $18.66 \mu\text{g h}^{-1} \text{mg}^{-1} \text{cat.}$ and a FE of 9.04% in NRR test. During

the discharge of the Al- N_2 battery, an NH_3 yield of $13.47 \mu\text{g h}^{-1} \text{mg}^{-1} \text{cat.}$ and a FE of 5.06% were also obtained. A series of control experiments showed that the excellent catalytic performance came from the hollow structure that promoted the diffusion of reactants and exposed more active sites, as well as the promotion of proton transfer by phosphate. In the same year, they developed hollow cobalt phosphate microsphere (CoPi/HSNPC) as a dual-function catalyst for Zn- N_2 batteries.^[136] Due to the enhanced proton conduction and numerous active sites, the CoPi/HSNPC obtained an NH_3 yield of $16.48 \mu\text{g h}^{-1} \text{mg}^{-1} \text{cat.}$ and a high FE of 4.46%, and the FE can be further increased to 24.42% when used as a Zn- N_2 battery. These studies offer guiding significance for the development of other metal phosphate catalysts, and provide new insights into the design of nitrogen fixation devices under mild conditions.

In addition to spherical hollow structural catalysts, tubular structural catalysts with hollow cylindrical structures have also been developed as NRR catalysts. They not only have the

advantages of various hollow structural materials, but also provide fast mass transfer channels. Most recently, β -cobalt phthalocyanine nanotubes (CoPc NTs) were developed on a large scale by Ghorai et al. to improve the activity and selectivity for NRR (Figure 6c).^[137] The tubular hollow structural material not only provided a high specific surface area ($41.5 \text{ m}^2 \text{ g}^{-1}$) to expose abundant active sites, but also served as a mass transfer channel for NRR. Studies have found that nonmetallic phthalocyanine can effectively reduce the hydrogen adsorption capacity of transition metal Co. The NRR test was carried out in 0.1 M HCl electrolyte, and the prepared CoPc NTs obtained an ultrahigh NH_3 yield of $107.9 \mu\text{g h}^{-1} \text{ mg}^{-1}_{\text{cat}}$ and an excellent FE of 27.7% at -0.3 V versus RHE. The $^{15}\text{N}_2$ isotope tracer experiments have confirmed that the NH_3 production was the result of N_2 reduction rather than the contamination caused by the N-contained in the material itself, which was very convincing characterization for the N-containing catalysts. Notably, CoPc NTs had bon electrocatalytic selectivity as well as structural stability, which were also important criteria to evaluate excellent catalysts. The density functional theory (DFT) calculation results indicated that cobalt with a low d-band center value was the main active site of catalysis, and associative alternating pathway was the preferred pathway for CoPc NTs. In conclusion, the effective inhibition of the hydrogen adsorption of transition metals by nonmetallic phthalocyanines, the enhancement of mass transfer by the tubular hollow structure, and the activation of $\text{N}\equiv\text{N}$ by the d orbital of Co are considered to be key factors for the excellent performance. These results provide guidance for the further development and design of phthalocyanine catalysts based on other transition metals.

Compared with other hollow structural materials, cubic hollow structural material with sharp edges has a larger specific surface area, as shorter ion transport path, and more unsaturated surface atoms, which is considered to be a more effective catalyst. El-Sayed and co-workers^[31] prepared hollow porous gold nanocages (AuHNCs) using silver nanocubes as templates by the galvanic replacement method (Figure 6d). AuHNCs exhibited an excellent FE of up to 30.2% in the 0.5 M LiClO_4 electrolyte at -0.4 V versus RHE, and the highest NH_3 yield of $3.98 \mu\text{g cm}^{-2} \text{ h}^{-1}$ was achieved at -0.5 V versus RHE. At a more negative potential, the active sites were more likely to be occupied by hydrogen than nitrogen due to the influence of competitive HER, leading to a significant drop in the FE and NH_3 yields. After five consecutive cycles, the catalytic performance of the AuHNCs was maintained at about 93.8%, which demonstrated the durability of the AuHNCs. Noteworthy, the NH_3 yields for Au nanospheres (diameter 35 nm) and Au nanocubes (AuNCs, side length 35 nm) were slightly increased than that for Au nanorods (length 42 nm and width 12 nm), as shown in Figure 6e. This result indicates that materials with sharper edges have more unsaturated surface atoms, which can provide more active sites than those with smooth surfaces. In addition, the enhanced catalytic performance of AuHNCs over AuNCs is attributed to the fact that N_2 molecules can be trapped by their cavities, which would extend the residence time of N_2 molecules on the inner surface of the catalyst, thus facilitating the conversion of N_2 to NH_3 .

The limitation of the cavity on reactants enables the hollow structural material to possess enhanced selectivity, and therefore, reasonable design of the pore size is very important. For pore

with extreme small size, it is difficult for reactants to enter into the cavity, while for pore with large pore size, it is difficult for the cavity to maintain the restriction effect on the reactants. Nazemi and El-Sayed explored the influence of the pore size of hollow structural materials on the performance of NRR.^[138] AuHNCs (AuHNC-635, AuHNC-715, AuHNC-795) with different peak localized surface plasmon resonances (LSPRs) were prepared by adding different amounts of Au^{3+} to replace the Ag nanocubes (Figure 6f–h). They found that as the LSPR became larger, the pore size of the nanocage increased. It is worth noting that a further increase in the pore size of the catalysts reduced the catalytic activity, due to the excessive reduction of the active surface area and the weakening of restricted ability of reactants. Compared with AuHNC-635 and AuHNC-795, AuHNC-715 displayed the best catalytic performance with NH_3 yield of $3.74 \mu\text{g h}^{-1} \text{ cm}^{-2}$ and FE of 35.9%. Hence, the design of the pore size of the hollow catalysts should conform to the characteristics to guarantee the diffusion of reactants and products without excessive loss of surface area.

To sum up, hollow structural materials are promising NRR catalysts due to their advantages of large specific surface area, rapid mass transfer, and restriction of reactants. In order to obtain better catalytic performance, pore size and morphology of the hollow structural material should be optimized. In addition, although there has not been a detailed study on the impact of the shell thickness of hollow structural materials on the catalytic performance of NRR, it is conceivable that the shell thickness would have a certain impact on the exposure of catalytic active sites. At the same time, it is also worth exploring that the modified or hybrid hollow structural materials possess stronger roughness and can expose more N_2 adsorption sites than smooth hollow structural materials. Furthermore, some complex multishell hollow structural materials with enhanced reactant confinement capabilities are worth further exploration, which may further improve the catalytic performance of NRR.

4.2. Mesoscopic Regulation of Hollow Structural Catalysts

Although the intrinsic hollow structural catalysts have various considerable advantages, the rational design of composite materials constructed with hollow structural materials as substrates may result in efficient catalysts with enhanced performance. Hollow structural materials with large specific area and high stability are suitable carriers to load other active ingredients efficiently and stably by the postsynthetic means or the impregnation method. The large specific surface area allows the hollow structural material to load more active ingredients, thereby upgrading N_2 adsorption sites. The high structural stability enables the hollow structural materials to prevent the structure from being collapsed or destroyed when loading other active ingredients, and effectively averts the agglomeration of active sites. Meanwhile, the excellent electrolyte diffusion channel provided by hollow structural materials can also bring better N_2 accessibility to the active components. Moreover, the adjustment of the interfacial electrons and the enhanced electron transfer between different components can further optimize the catalytic activity of NRR. Therefore, it is an effective method to further optimize the hollow structural catalysts under the mesoscopic level.

The term “mesoscopic” refers to the intermediate state between “macroscopic” and “microscopic,” and is applied in microstructures with the characteristics of crossover and intersection between quantum state and classical state. Therefore, mesoscopic materials endow nanomolecules and nanomaterials with specific properties, providing broad applications. Commonly, the mesoscopic materials refer to nanomaterials that have at least 1D between 1 and 100 nm on the 3D scale, and they are often used as building blocks to participate in the formation of materials. In the past few decades, studies have found that metallic materials with nanoscale dimensions belong to mesoscopic materials. In this state, metallic nanomaterials possess unique localized surface plasmon (LSP) effects, small size effects, and surface effects.^[139,140] LSP effects play a key role in enhancing the electric field on the surface of nanoparticles, small size effects play role in increasing the specific surface area, and the surface effects play role in altering surface energy and surface binding energy of nanoparticles. Combining these unique properties, mesoscopic materials as electrocatalysts exhibit excellent NRR performance. According to different regulation methods, the mesoscopic regulation of hollow structural materials is simply divided into two categories: hollow structural materials as carriers to load nanomaterials and hollow structural materials as substrates to construct heterostructures by coupling with other components.

4.2.1. Loading Nanomaterials

The catalytic activity of electrocatalysts is related to the size of the nanomaterials. The smaller the size, the larger proportion of surface active atoms the nanomaterials will have, which makes nanoscale materials to have potential as catalysts. However, nanomaterials with extreme small size commonly possess high surface-unsaturated coordination and enhanced surface energy, which would result in uncontrolled spontaneous agglomeration. Therefore, it is necessary to find a suitable carrier to anchor the highly active nanomaterials to prevent their agglomeration.

The hollow structural material is considered to be a good carrier due to its large specific surface area and high surface-unsaturated coordination, which can support and disperse various nanoparticles, such as nanoparticles, molecules, and quantum dots. On this basis, tubular hollow structural materials with continuous interconnecting ion diffusion paths and enhanced permeability have attracted much attention. Carbon nanotubes (CNTs), as a typical tubular hollow structural material, have been widely used in the fields of energy storage and energy conversion.^[141,142] Although CNTs have a very low catalytic activity ($\approx 1 \mu\text{g h}^{-1} \text{mg}^{-1}_{\text{cat}}$) during electrocatalytic reactions,^[143] their excellent conductivity, large specific surface area, and high surface unsaturated coordination make them excellent catalyst carriers, which could load and disperse the nanoparticles uniformly and stably. Ding and co-workers reported iron phthalocyanine/oxidized multiwalled carbon nanotubes (FePc/O-MWCNT) as NRR catalysts by dispersing FePc on O-MWCNT.^[144] At -0.3 V versus RHE, FePc/O-MWCNT exhibited a FE of 9.73% and an NH_3 yield of $36 \mu\text{g h}^{-1} \text{mg}^{-1}_{\text{cat}}$, which were better than pure FePc and O-MWCNT. Fe_3C also could be considered as an effective NRR catalyst. Huang and co-workers prepared N-doped carbon nanotube/ Fe_3C nanoparticle through a simple pyrolysis

method.^[145] The results show that: 1) CNTs could effectively increase the specific surface area of the catalyst; 2) Fe_3C acted as the active center of the NRR catalyst; 3) the high content of pyridine nitrogen not only contributed to N_2 adsorption, but also improved the hydrophilicity of the catalyst. Li et al. used MWCNT as a carrier to anchor CuCo_2S_4 and prepared $\text{CuCo}_2\text{S}_4/\text{MWCNT}$ as a highly efficient NRR catalyst.^[146] CuCo_2S_4 nanoparticles were known to easily self-agglomerate without carriers to form particles ranging from 200 to 300 nm in size. The introduction of MWCNT effectively changed the dispersion of CuCo_2S_4 to a particle size of 30–50 nm, which exposed more active sites. In addition, the introduction of MWCNT also increased the specific surface area of the catalyst and improved the electron transfer capacity. $\text{CuCo}_2\text{S}_4/\text{MWCNT}$ obtained a high NH_3 yield of $137.5 \mu\text{g h}^{-1} \text{mg}^{-1}_{\text{cat}}$ and a corresponding FE of 8.7% in 0.1 M Na_2SO_4 electrolyte.

Ru catalyst is considered structure-sensitive for NRR by DFT because Ru metal could increase the binding strength of N_2 and lower the energy barrier for N_2 detachment. It is effective to seek a suitable substrate for Ru dispersion to improve the atomic utilization. Recently, Ma and co-workers assembled ruthenium polyethyleneimine (Ru-PEI) onto carboxyl-modified CNTs by electrostatic force and prepared Ru-PEI@MWCNTs as an efficient NRR catalyst (Figure 7a).^[147] No aggregated particles were found by scanning electron microscopy (SEM) and transmission electron microscopy (TEM), which confirmed that MWCNTs could uniformly disperse Ru-PEI. As shown in Figure 7b, a large number of bright spots were found in the high-resolution TEM (HRTEM) image, which further confirmed the uniform loading of Ru-PEI. Further research found that PEI with abundant NH_2 groups had strong coordination ability, which was key to the stable and efficient loading of Ru-PEI on MWCNTs. It was difficult to load substantial Ru on MWCNTs without introducing PEI. As shown in Figure 7c, the carefully designed Ru-PEI@MWCNTs exhibited a high ammonia yield of $188.9 \mu\text{g h}^{-1} \text{mg}^{-1}_{\text{cat}}$ and an excellent FE of 30.93%, which were better than other comparative samples.

Although CNTs have many advantages as substrates, their low NRR catalytic activity hinders the efficient production of NH_3 . Therefore, the development of active hollow substrate is particularly important. Wu and co-workers reported the composite $\text{Mn}_3\text{O}_4/\text{blue titanium dioxide (b-TiO}_2)$ as an efficient NRR catalyst, which was prepared by depositing Mn_3O_4 nanoparticles on b-TiO₂ nanotubes (Figure 7d).^[148] It was found that different loading amounts exerted an impact on the catalytic activity of the catalysts. When the loading capacity of Mn_3O_4 was 0.57 mg cm^{-2} ($0.57\text{Mn}_3\text{O}_4/\text{b-TiO}_2$), the catalyst exhibited the best NRR performance with NH_3 yield of $1.61 \times 10^{-10} \text{ mol s}^{-1} \text{ cm}^{-2}$ at -0.45 V versus RHE. As the loading amount of Mn_3O_4 further increased, excessive Mn_3O_4 aggregated and caused blockage of TiO₂ nanotubes, resulting in a decrease in specific surface area, thereby reducing the catalytic performance. In addition, the excellent performance of $0.57\text{Mn}_3\text{O}_4/\text{b-TiO}_2$ came from not only the simple superposition of $0.57\text{Mn}_3\text{O}_4$ and b-TiO₂, but also the limiting effect of nanotube cavity on the intermediate, thereby effectively improving the NRR reaction kinetics (Figure 7e). As shown in Figure 7f,g, finite element analysis was used to simulate the distribution of intermediate concentration in nanotube and planar mode. The results showed that nanotube can effectively limit the

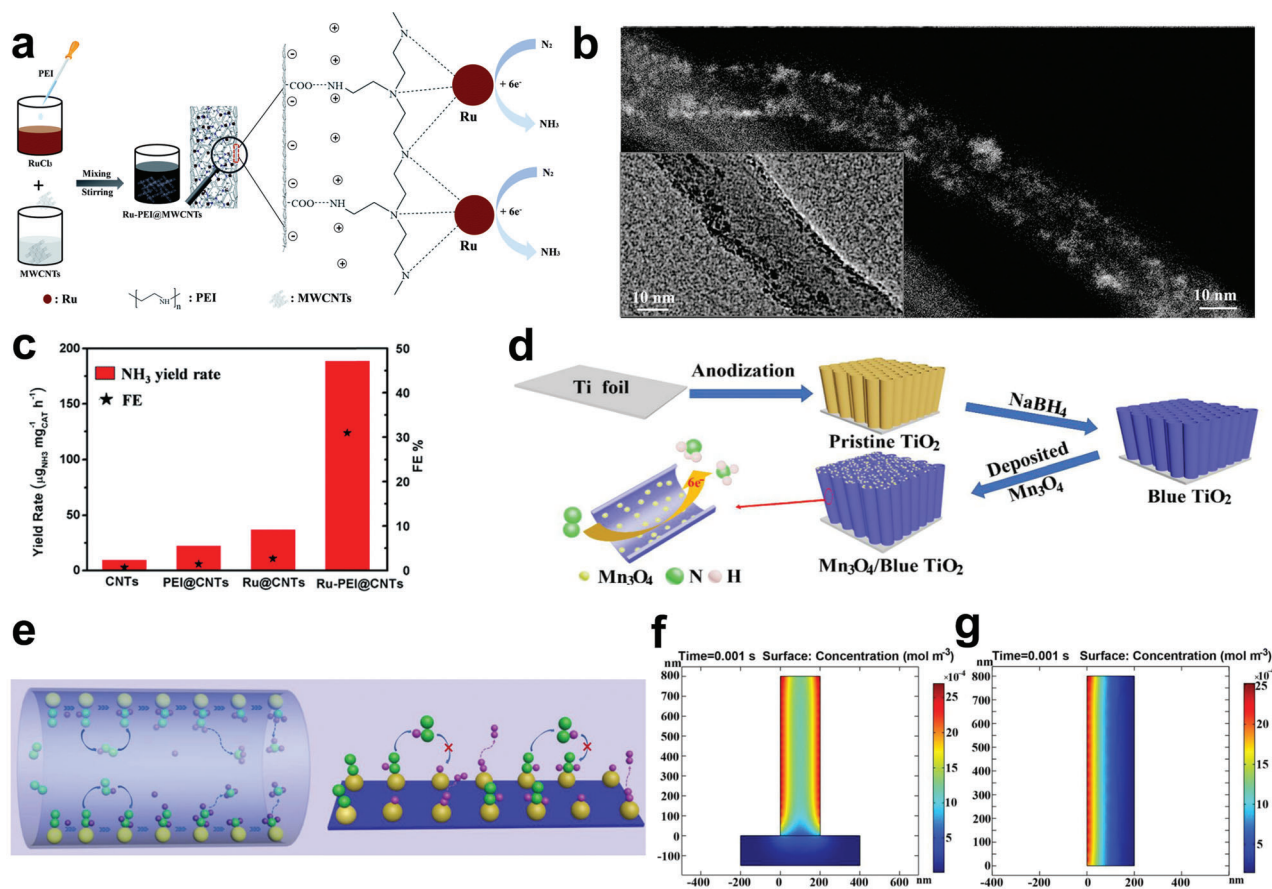


Figure 7. a) Schematic illustration of the synthetic process of Ru-PEI@MWCNTs. b) HRTEM image of Ru-PEI@MWCNTs. c) NH₃ yields and FEs of different catalysts. Reproduced with permission.^[147] Copyright 2019, Royal Society of Chemistry. d) Schematic illustration of the fabrication of Mn₃O₄/b-TiO₂ nanotube arrays. e) Schematic of reaction intermediates confined in nanotube and planar models. f) Concentration of *N₂ intermediates for nanotube model. g) Concentration of *N₂ intermediates for planar model. Reproduced with permission.^[148] Copyright 2020, Wiley-VCH.

reaction intermediates and increase the local intermediate concentration, while the plane is difficult to limit the intermediates.

Black phosphorus has attracted wide attention due to its excellent electrochemical properties, among which the quantized one shows good catalytic activity. However, pure black phosphorous quantum dots (BP QDs) will inevitably undergo agglomeration, which will cause the loss of active sites. For this reason, Ding and co-workers successfully self-assembled BP QDs onto tin dioxide nanotubes reduced by sodium borohydride (BP@SnO_{2-x}) through tin-phosphorus coordination interactions.^[149] At -0.4 V versus RHE, BP@SnO_{2-x} showed the highest NH₃ yield of 48.87 μg h⁻¹ mg⁻¹_{cat.} and a FE of 14.6%, which were better than individual BP QDs (29.22 μg h⁻¹ mg⁻¹_{cat.}) and SnO_{2-x} (8.64 μg h⁻¹ mg⁻¹_{cat.}), respectively. In addition, after a long-term electrolytic experiment, BP QDs were still stably loaded on SnO_{2-x} without agglomeration, indicating that BP@SnO_{2-x} had excellent stability.

4.2.2. Construction of Heterostructures

Heterojunction refers to the junction or interface between different materials, that is, the crystal interface formed by the combi-

nation of two materials with different bandgaps. Therefore, heterostructure is defined as a structure with more than two layers containing a heterojunction. Compared with a single component, the interface in heterostructure is conducive to increasing active sites and electronic regulation, thereby playing an important role in improving the catalytic performance.^[150,151] Meanwhile, the heterostructure can speed up the electron transfer due to electronegative differences between dissimilar components, further facilitating the adsorption/desorption of reaction intermediates.^[152,153] In addition, different components can play separate roles, thereby synergistically optimizing catalytic performance.^[154,155] Among them, the hollow structural material can be used as a carrier loading other nanomaterials to construct a heterostructure catalyst, which can achieve rapid mass diffusion and effectively reduce the overpotential.^[156,157] Furthermore, the structural stability of the hollow structural material can reduce the agglomeration of active materials during the reaction and maximize the exposure of active sites.^[158-160]

Wang and co-workers reported NiCoS/C nanocage, where NiCoS and C possessed strong chemical coupling effect.^[161] This nanocage was obtained by vulcanizing NiCo-layered double hydroxide (LDH)@ZIF-67, exhibiting a high NH₃ yield of 58.5 μg h⁻¹ mg⁻¹_{cat.} and a FE of 12.9% at 0.1 M Li₂SO₄ (Figure 8a). The

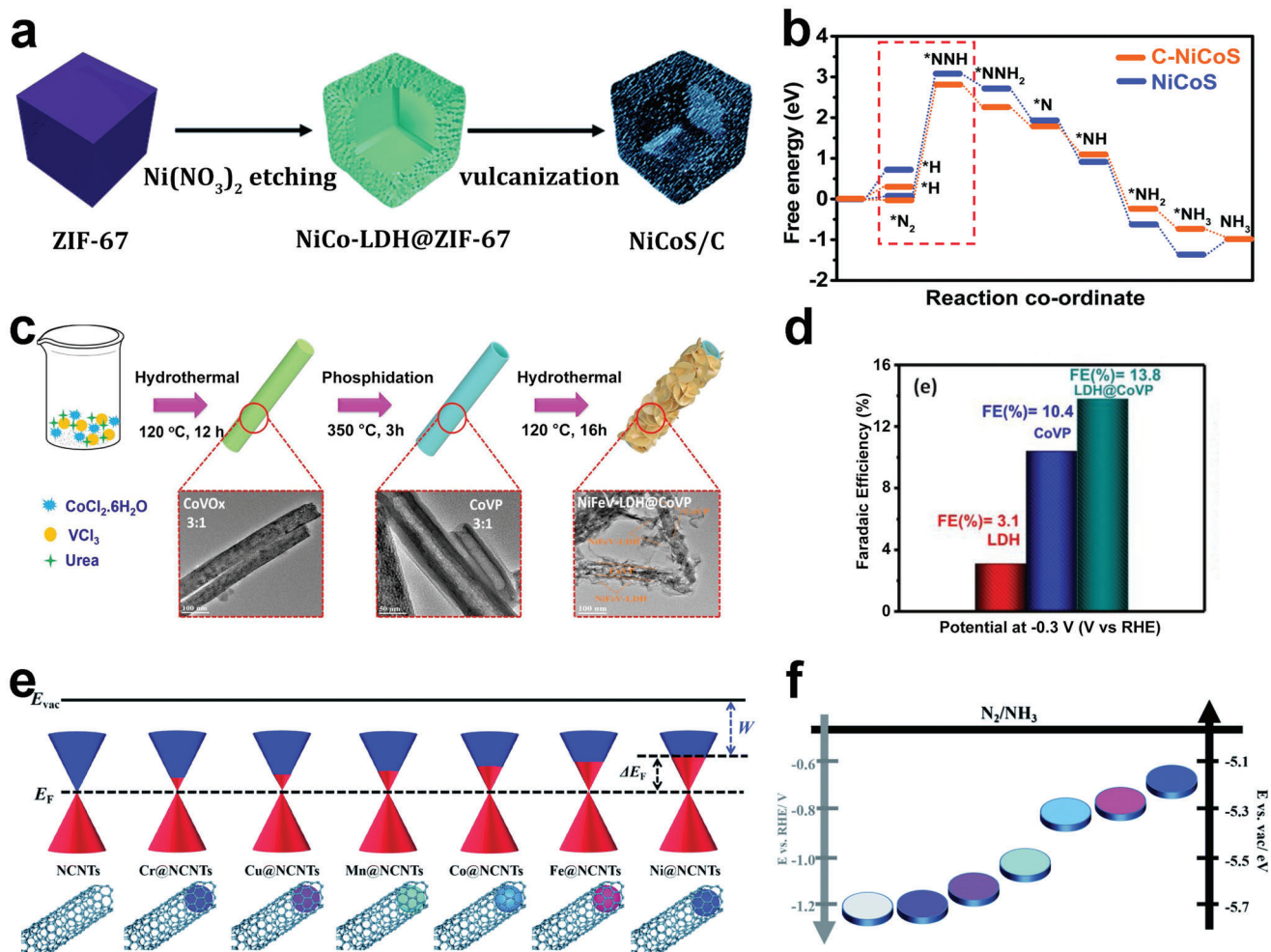


Figure 8. a) Schematic illustration of the formation process of NiCoS/C nanocage. b) Free energy diagram of N_2 reduction on NiCoS/C and NiCoS. Reproduced with permission.^[161] Copyright 2020, Royal Society of Chemistry. c) Schematic diagram for the synthetic procedure of CoVP@NiFeV-LDHs. d) FEs for NiFeV-LDHs, CoVP, and CoVP@NiFeV-LDHs. Reproduced with permission.^[162] Copyright 2020, Elsevier. e) Schematic illustration of the design concept of work function of M@NCNTs. E_{vac} and E_{F} represent vacuum level and Fermi level, respectively. f) The corresponding energy level diagram. Reproduced with permission.^[163] Copyright 2020, Royal Society of Chemistry.

nitrogen temperature-programmed desorption (N_2 -TPD) confirmed that NiCoS/C nanocage exhibited enhanced N_2 adsorption capacity compared with a single NiCoS nanocage prepared by prolonging the vulcanization time. In addition, the NiCoS/C nanocage was prior to NiCoS in terms of structural stability and HER inhibition ability. The DFT calculations further confirmed that the coupling interaction between NiCoS and C could reduce the free energy barrier in the NRR rate-determining step (Figure 8b). This research provides new ideas for the design and development of polymetallic hollow heterostructural materials as NRR catalysts.

Electrocatalytic NRR is considered to be a PCET reaction. In this reaction, the adsorption of N_2 molecules on the active site and the subsequent activation by accepting electrons are believed to be important steps. Since the complete reduction of N_2 to NH_3 requires N_2 activation and 6-electron PCET reaction, good electrical conductivity and fast electron transfer are also important criteria for evaluating catalysts. The heterostructures play a unique

role in accelerating interfacial charge transfer and enhancing electrical conductivity. Typical LDH nanosheets possessing large surface areas can expose more active sites, but their electrical conductivity is relatively poor. To address this issue, Yan and co-workers reported a heterogeneous structure CoVP@NiFeV-LDHs with accelerated interfacial charge transfer and enhanced conductivity by loading NiFeV-LDHs on CoVP hollow nanotubes (Figure 8c).^[162] Electrochemical impedance spectroscopy analysis verified that the heterostructure of CoVP@NiFeV-LDHs had the best electron transport capability relative to single-component CoVP and NiFeV-LDHs. The hollow CoVP nanotubes not only enhanced the diffusion kinetics of NRR, but also provided structural stability for the dispersion of NiFeV-LDHs. In the $0.05\text{ M H}_2\text{SO}_4$ electrolyte, the finely designed CoVP@NiFeV-LDHs obtained the highest NH_3 yield of $1.6 \times 10^{-6}\text{ mol h}^{-1}\text{ cm}^{-2}$ at -0.3 V versus RHE. As shown in Figure 8d, CoVP@NiFeV-LDHs demonstrated the highest FE (13.8%) relative to CoVP (10.4%) and NiFeV-LDHs (3.1%). In addition,

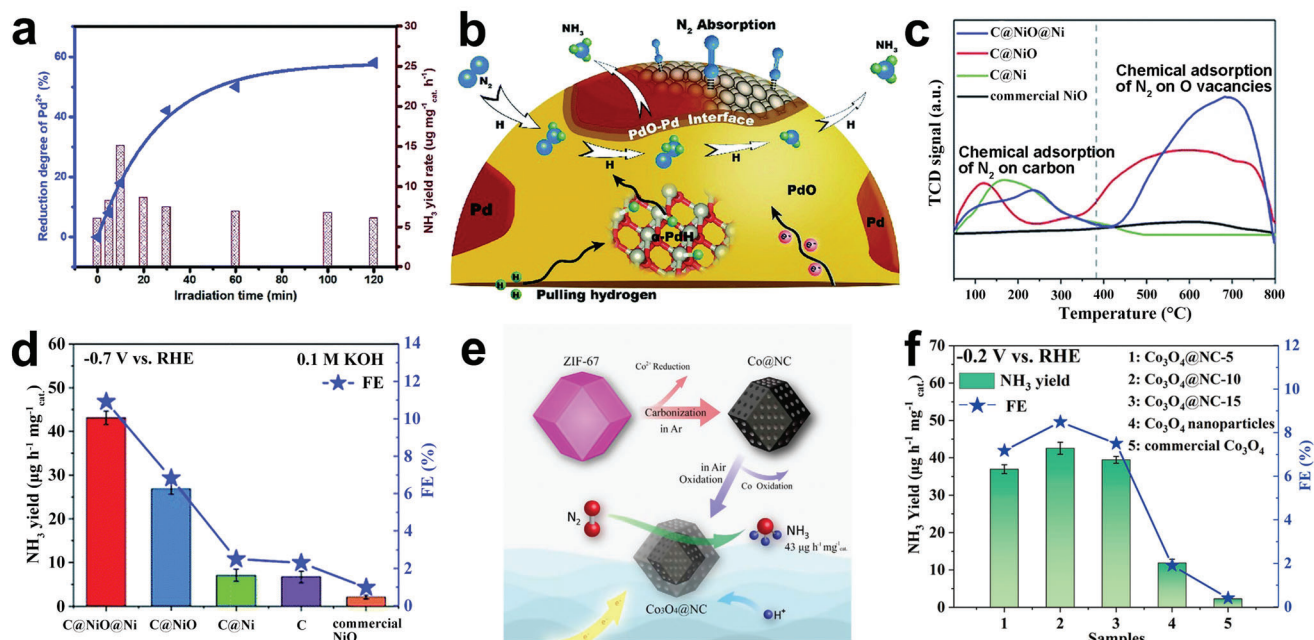


Figure 9. a) Reduction degree and NH₃ yield rates of PdO/CNTs with different irradiation times. b) Alternative hydriding pathway for NRR on the PdO–Pd interface. Reproduced with permission.^[164] Copyright 2019, Royal Society of Chemistry. c) N₂-TPD profiles of different catalysts. d) NH₃ yield rates and FEs of different catalysts at –0.7 V versus RHE. Reproduced with permission.^[165] Copyright 2020, Royal Society of Chemistry. e) Schematic illustration of the preparation of core–shell Co₃O₄@NC. f) NH₃ yield rates and FEs of different catalysts at –0.2 V versus RHE. Reproduced with permission.^[166] Copyright 2019, American Chemical Society.

CoVP@NiFeV–LDHs also had good stability, as evidenced by no obvious performance degradation after 8 consecutive cycles.

Recently, Zhang and co-workers designed a series of metal-encapsulated N–CNT Schottky heterojunctions as NRR catalysts, and systematically studied the regulation of work function on catalytic activity.^[163] As shown in Figure 8e, the work functions of M@NCNTs decreased in the order of metal M being Cr, Cu, Mn, Co, Fe, Ni, with NCNTs having the highest work function and Ni@NCNTs having the lowest work function. As shown in Figure 8f, the energy required to drive the NRR reaction dropped as the work function decreased. Ni@NCNT was therefore considered as the most promising and high-efficient NRR catalyst. The correction of the charge density of this Mott–Schottky heterostructure was further proved by comparing the peak shift of the pyridine nitrogen in the X-ray photoelectron spectroscopy (XPS) spectrum. The finely designed Ni@NCNTs obtained the highest NH₃ yield of 53.88 μg h⁻¹ mg⁻¹ cat. and the maximum FE of 7.33% at –0.5 and –0.3 V versus RHE, respectively. All in all, the decrease in work function can increase the charge density near the Fermi level, thereby accelerating electron transfer to promote the activation of N₂. The above studies show that researchers should pay attention to the electron-supply capacity of catalysts while improving their activity.

In addition to improving the conductivity of the catalyst and accelerating electron transfer, the construction of heterostructures can also form a unique heterogeneous interface to promote the adsorption of reactants and finally improve the catalytic activity. Among them, the metal–metal oxide interface is considered to be the best choice for improving the catalytic activity due to the strong interfacial interaction force between them. By adjusting

the laser irradiation time, Liang and co-workers partially reduced the PdO nanoparticles grown on CNTs to Pd, forming PdO/Pd heterojunction CNTs (PdO/Pd/CNTs).^[164] As shown in Figure 9a, the irradiation time determined the reduction degree of Pd²⁺, which directly affected the NRR performance. Among them, the sample irradiated for 10 min showed the highest NH₃ yield (18.2 μg h⁻¹ mg⁻¹ cat.). As shown in Figure 9b, when N₂ reached the PdO/Pd heterogeneous interface, Pd would capture N₂ to form Pd–N bond, while adjacent PdO would form α-PdH with activated protons, shortening the subsequent proton transfer distance and effectively reducing the overpotential of NRR. Coincidentally, Luo et al. used Ni-based MOF to derive C@NiO@Ni microtubes by adjusting the annealing method as an efficient NRR catalyst under alkaline conditions, showing high NH₃ yield (43.15 μg h⁻¹ mg⁻¹ cat.) and FE (10.9%).^[165] Both electron paramagnetic resonance (EPR) and XPS spectra confirmed the rich oxygen vacancies in C@NiO@Ni and C@NiO. As shown in Figure 9c, N₂-TPD demonstrated that oxygen vacancy could enhance the chemical adsorption capacity of N₂, indicating that oxygen vacancy was the active site of the catalyst. Although oxygen vacancies existed, the abundant NiO/Ni interface in alkaline electrolyte was proven to be more critical for proton capture to further promote the NRR reaction. As shown in Figure 9d, C@NiO@Ni exhibited NH₃ yield that was 0.62 times higher than C@NiO, which was much higher than C@Ni, C, and commercial NiO. However, the oxygen vacancy concentration of C@NiO@Ni is only 0.23 times higher than the oxygen vacancy concentration of C@NiO. The performance difference was probably due to the influence of the NiO/Ni interface. This work develops complex catalytic systems and emphasizes the importance of detailed characterization

of the contribution of each component, which guides researchers to explore multifunctional electrocatalysis.

Core-shell structure is also a typical heterostructure, which has the advantages of adjustable size, large specific surface area, and unique core-shell interface. In some cases, a stable outer shell can act as a protective layer to protect the inner core from erosion. On this basis, the core-shell structure with hollow characteristics enables the fast capture of reactants. Wang and co-workers prepared $\text{Au}_3\text{Cu}@Cu$ nanocages with a hollow porous core-shell structure using Cu_2O as a template, which demonstrated a high NH_3 yield of $33.97 \mu\text{g h}^{-1} \text{mg}^{-1}_{\text{cat}}$ and an excellent FE of 21.41% at 0.1 M Na_2SO_4 .^[167] The hollow porous heterostructure effectively increased the specific surface area while limiting the reactant to increase the contact frequency between the active site and the reactant. At the same time, the outer layer of Cu readily inhibited competitive HER, which would improve the NRR selectivity. Recently, Luo et al. developed a N-doped carbon/ Co_3O_4 ($\text{Co}_3\text{O}_4@\text{NC}$) core-shell structure derived from ZIF-67 for the first time, as shown in Figure 9e.^[166] The materials with different morphologies ($\text{Co}_3\text{O}_4@\text{NC-5}$, $\text{Co}_3\text{O}_4@\text{NC-10}$, $\text{Co}_3\text{O}_4@\text{NC-15}$) were prepared at different calcination times (5, 10, 15 h) under air atmosphere due to different migration rates. As the oxidation time increased, the degree of graphitization and specific surface area of $\text{Co}_3\text{O}_4@\text{NC}$ increased. In this work, oxygen vacancies were also considered to be a key factor in determining catalytic performance, because they can inject captured metastable electrons into the antibonding orbital of N_2 to weaken $\text{N}\equiv\text{N}$. Finally, the core-shell structure $\text{Co}_3\text{O}_4@\text{NC-10}$ with the highest oxygen vacancies obtained the best NRR performance (NH_3 yield: $42.58 \mu\text{g h}^{-1} \text{mg}^{-1}_{\text{cat}}$, FE: 8.5%) compared to its counterpart and Co_3O_4 nanoparticles, as shown in Figure 9f. This work encourages researchers to combine multiple advantages into one catalyst, which may play an unexpected role in synergistically promoting NRR. It is equally important that this synergistic effect needs to be explored in depth to clarify their respective contributions.

In short, the fine edge exposed part of heterostructures can provide more adsorption sites for N_2 . In terms of structures, the hollow heterostructures have both the advantages of enhanced conductivity of the heterojunctions and rapid mass diffusion of hollow structures. In terms of materials, heterostructural materials can integrate the advantages of different components, thereby optimizing catalytic performance. It is worth noting that the excellent catalytic performance of heterostructural materials is often attributed to the synergy between different components. However, this synergy needs to be further investigated in detail to clarify their internal mechanism.

4.3. Microscopic Regulation of Hollow Structural Catalysts

In addition to mesoscopic regulation methods, the catalytic performance of hollow structural catalysts can be further improved through microscopic regulation strategies. Here, microscopic regulation is defined as the control of at least 1D size of materials in the 3D space on the atomic scale in the range of 0.1–1 nm. Compared with mesoscopic regulation, microscopic regulation is more inclined to atomic-level control to enhance the inherent activity of the catalysts. The hollow structural catalysts

can be modified in favor of NRR through various microscopic regulation strategies. For example, after microscopic regulation, the local coordination environment of hollow structural materials will be adjusted to improve the affinity between the catalyst and N_2 . Meanwhile, the electronic structure, electron transmission, and conductivity can be optimized and surface defects can be created through microscopic regulation. In conclusion, microscopic regulation strategies render the hollow structural catalysts more excellent catalytic performance. Considering the different regulation methods, the microscopic regulation of hollow structural materials is simply divided into the following categories: doping engineering, vacancy engineering, single atom engineering, etc.

4.3.1. Doping Engineering

The heteroatom doping is an effective strategy to regulate the physical or chemical properties of materials because heteroatoms and intrinsic atoms have different electronic structures. The introduction of heteroatoms will create a special coordination environment on the surface of the materials, adjust the electronic structure, and manufacture defects, which will help increase the active sites and improve the binding ability with N_2 . Therefore, heteroatom doping is considered as an effective method to improve catalytic activity and has been widely studied in the field of electrocatalytic NRR. For example, Sun and co-workers synthesized Fe-doped TiO_2 as a NRR catalyst, which showed 5 times higher NH_3 yield than undoped TiO_2 .^[168] The introduction of iron spontaneously increased the oxygen vacancy content in the TiO_2 , which was thought to be the active site that promoted N_2 activation. Zhang and co-workers designed a dual-function catalyst Fe-doped SnO_2 , which exhibited very excellent catalytic performance compared to undoped SnO_2 .^[169] Experiments and DFT calculations indicated that a part of the introduced heteroatom Fe was doped into the crystal lattice to improve the conductivity of SnO_2 , and other parts were anchored in the oxygen vacancy to form single-atom Fe to enhance the adsorption and activation of N_2 . Quan and co-workers prepared N-doped porous carbon as NRR cathode material by pyrolysis of ZIF-8.^[170] Studies have found that N doping adjusted the electronic structure of the material and induced charge polarization, in which pyridinic N and pyrrolic N were the active sites for N_2 adsorption and activation.

As an excellent strategy, heteroatom doping has also been applied to further enhance the catalytic activity of hollow carbon materials. The heteroatom doping of carbon-based hollow structural materials can create defects, adjust the electronic structure, and increase the number of active sites. Sun and co-workers prepared S-doped carbon nanospheres (S-CNSs) as an excellent NRR catalyst by hydrothermal treatment.^[171] Raman spectra showed that S-CNSs had higher disorder degree and more defects than undoped carbon nanospheres (CNSs). N_2 -TPD revealed that S-CNSs had stronger chemical and physical adsorption capacity for N_2 . Also, S-CNS achieved a high NH_3 yield of $19.07 \mu\text{g h}^{-1} \text{mg}^{-1}_{\text{cat}}$, which was more than 5 times higher than CNS. Recently, Hu and co-workers synthesized P-doped carbon nanotubes (P-CNTs) as NRR electrocatalyst through simple grinding and temperature-assisted phosphorization.^[172] In 0.25 M LiClO_4 , the P-CNTs showed a high NH_3 yield of $24.4 \mu\text{g h}^{-1} \text{mg}^{-1}_{\text{cat}}$ at -1.1 V versus RHE and a FE of 12.5% at -0.3 V

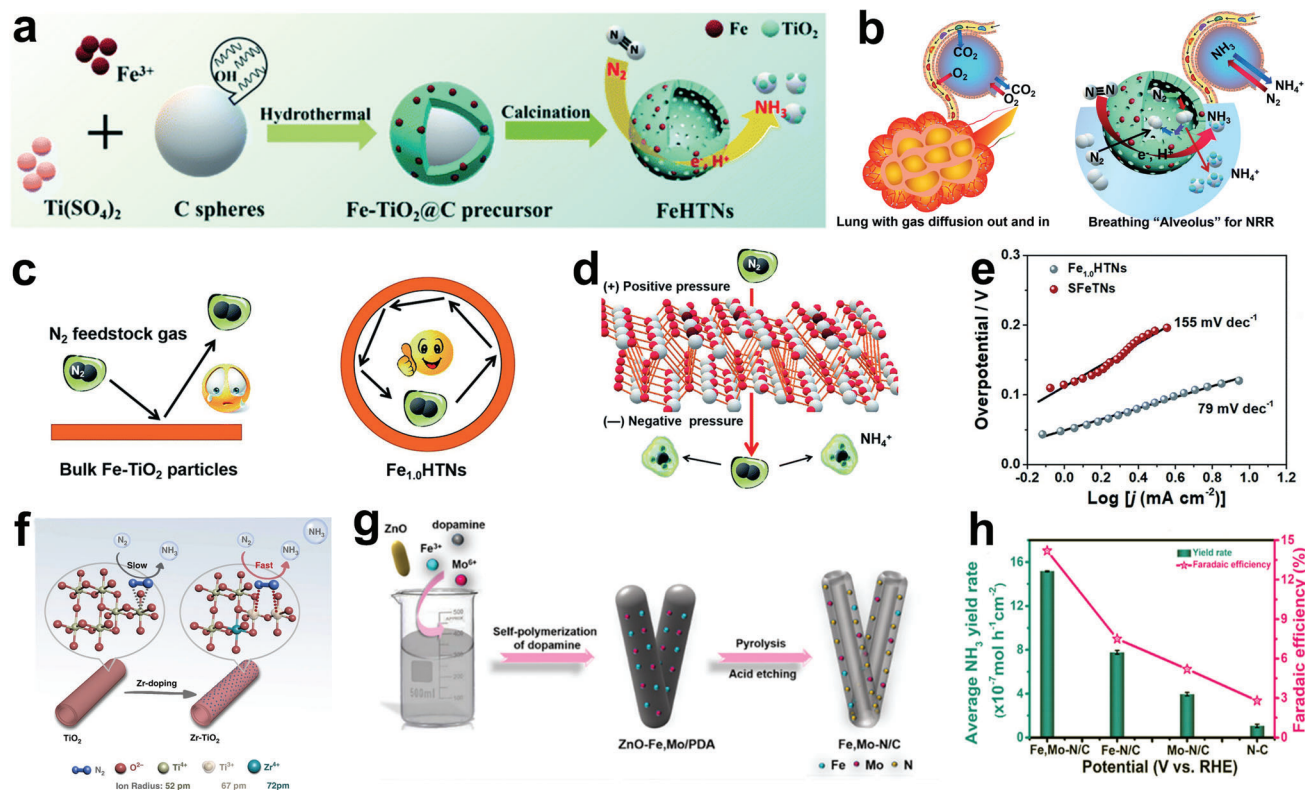


Figure 10. a) Schematic diagram of the synthesis of FeHTN. b) Left: scheme of a human lung and a single alveolus. Right: schematic illustration of an artificial breathing “alveolus” of FeHTNs for NRR. c) Schematic of the collision behaviors of N_2 on the surfaces of different samples. d) Schematic of pressure differences inside and outside the cavity of $Fe_{1,0}HTN$. e) Tafel plots of different samples for NRR. Reproduced with permission.^[174] Copyright 2021, Royal Society of Chemistry. f) Schematic illustration of formation of adjacent bi- Ti^{3+} sites and oxygen vacancies owing to Zr doping in anatase TiO_2 . Reproduced with permission.^[175] Copyright 2019, Springer Nature. g) Scheme illustration of the synthetic process of Fe,Mo-N/C. h) NH_3 yields and FEs of different catalysts. Reproduced with permission.^[176] Copyright 2020, American Chemical Society.

versus RHE. Raman spectroscopy analysis found that P-CNTs had a higher I_D/I_G intensity ratio compared with the original CNTs, indicating that more defects were generated on the surface of P-CNTs. Control experiments found a linear relationship between NH_3 production and P doping, revealing that the P site was the true active center of NRR. The results of the Mulliken charge density redistribution showed that the heteroatom P contributed to the formation of Lewis acid sites to adsorb N_2 on the weak Lewis base due to its high positive charge density, which was an intuitive evidence that the P site was the reaction center. The free energy of N_2 adsorption on P atoms (-0.24 eV) was better than that on C atoms (-0.13 eV), further confirming that P was the active site of NRR. Eventually, the reaction followed an associative distal pathway which was demonstrated by UV and in situ infrared spectroscopy.

Metal-based hollow structural materials doped with heteroatoms have also been developed as electrocatalysts for NRR. The heteroatom doping of metal-based hollow structural materials can change the electronic structure and introduce vacancies, leading to enhanced reaction intermediates adsorption and rapid charge transfer.^[173] As shown in **Figure 10a**, Yuan and co-workers prepared Fe-doped titanium dioxide hollow nanospheres (FeHTNs) by a hard template method.^[174] HRTEM indicated that many oxygen vacancies existed in FeHTNs due to the boost-

ing of Fe doping. XPS spectroscopy and electron spin resonance both confirmed that Fe doping can increase the oxygen vacancy content of TiO_2 . FeHTNs with addition amount of 1.0 wt% Fe ($Fe_{1,0}HTNs$) exhibited a significantly enhanced NH_3 yield ($43.14 \mu g h^{-1} mg^{-1} cat.$), which was higher than that of undoped TiO_2 hollow nanospheres and solid Fe-doped TiO_2 nanoparticles (SFeTNs). Such excellent performance was attributed not only to the increase of oxygen vacancy content by Fe doping, but also to the hollow structural cavity that promoted N_2 absorption. As shown in **Figure 10b**, they proposed a concept of “alveolus,” similar to the breathing process of mammalian alveoli. Theoretical calculations showed that the number of N_2 collision on the surface of Fe-TiO₂ nanoparticles may be one, but the probability of N_2 collisions in the FeHTNs cavity would be multiple until NH_3 was formed (**Figure 10c**). Meanwhile, the discrepancy in the solubility of NH_3 causes the pressure difference between inside and outside the cavity to drive N_2 into the cavity (**Figure 10d**). In addition, compared to SFeTNs, $Fe_{1,0}HTNs$ had a higher Tafel slope value, which further confirmed the improvement of NRR kinetics due to the existence of the hollow structure (**Figure 10e**). The NRR performances of $Fe_{1,0}HTNs$ with different mechanically crushed times were compared. As the crushing time increased, the specific surface area of the material increased, but the catalytic performance continued to decline, which further

confirmed the significance of the cavity limiting effect to improve NRR properties.

Recently, Zheng and co-workers discovered that the adjacent bi-Ti³⁺ pairs formed on anatase TiO₂ were key sites for N₂ adsorption and activation using DFT calculations.^[175] As shown in Figure 10f, Zr-TiO₂ with the contiguous bi-Ti³⁺ pairs and oxygen vacancies was formed by doping the same valance dopant Zr⁴⁺ ions on anatase type TiO₂ nanotubes. In addition, Ce⁴⁺ with a larger ion radius could also be utilized as dopant (Ce-TiO₂) to produce oxygen vacancies, but it would be reduced to Ce³⁺ during the process of creating oxygen vacancies and may even destroy the crystal structure of TiO₂. The optimal NH₃ yield (8.90 μg h⁻¹ cm⁻²) of Zr-TiO₂ was obtained at -0.45 V versus RHE, which exceeded that of the undoped TiO₂ and Ce-TiO₂. The work calls for researchers to pay more attention to dopants with the same oxidation state. Very recently, Wang and co-workers prepared Pt-doped hollow iron phosphide nanorods (Pt-FeP/C) via derivatizing Pt-containing MIL-88A.^[177] DFT calculations revealed that Fe was the catalytic active center, P was an accelerator and proton provider for water splitting, and Pt doping effectively accelerated proton transfer. Compared with undoped materials, Fe doping will effectively reduce the energy barrier of the rate-determining step (*N₂ → *N₂H). In the end, the Pt-FeP/C obtained an NH₃ yield of 10.22 μg h⁻¹ cm⁻² and an excellent FE of 15.3% at relatively low voltage (-0.05 V), which was the highest NH₃ yield among the iron-based catalysts.

Reasonable selection of codopants can induce additional active sites for desirable catalytic performance, so heteroatom codoping is also an expected strategy. Yan and co-workers prepared Fe,Mo-codoped hollow porous carbon nanorods (Fe,Mo-N/C) using zinc oxide nanorods as templates (Figure 10g).^[176] Fe,Mo-N/C obtained the highest NH₃ yield of 1.52 × 10⁻⁶ mol h⁻¹ cm⁻² and the best FE of 14.2%, both of which were better than those of single Fe- or Mo-doped hollow porous carbon nanorods (Figure 10h). Such excellent performance should be attributed to the promotion of N≡N cleavage by Fe and Mo as active sites, the enhancement of N₂ adsorption by high pyridine nitrogen content in the material, and the high specific surface area of the hollow structural materials to enhance the exposure of active sites. Very recently, Chen and co-workers synthesized Ni-Fe-doped MoS₂ nanocages (Ni-Fe@MoS₂ NCs) using a self-template method for NRR.^[178] XPS confirmed that Ni-Fe codoping caused a large number of Mo-S bonds to break and then produced highly oxidized species, as well as abundant sulfur defects. DFT calculations showed that the active site of Ni_{0.3}Fe_{0.7} was key to accelerating electron transfer in NRR reaction. The spin-polarized density of state revealed that N₂ adsorbed on the active site of Ni_{0.3}Fe_{0.7} can easily obtain electrons provided by the S 2p and Mo 3d orbitals during the NRR process. As expected, Ni-Fe@MoS₂ NCs obtained an excellent NH₃ yield of 128.17 μg h⁻¹ mg⁻¹_{cat.} and a good FE of 11.34% at -0.3 V versus RHE.

In summary, doping heteroatoms can effectively adjust the electronic structure to enhance the N₂ adsorption, which inspires researchers to regulate efficient NRR catalysts through doping engineering. However, its development suffers from the following drawbacks. First of all, it is difficult to achieve a controllable doping amount and precise anchoring position. It is therefore urgently needed to develop reliable synthetic methods that can be mass-produced and possess universal applicability. This is partic-

ularly important for N-doped or N-containing materials to prevent the effects of doping on their stability and thus to avoid the generation of pollution sources that affect NRR results. Second, it is challenging to explore the relationship between doping types and activities and to precisely synthesize specific doping types. For example, N-doped carbon materials will produce nitrogen-containing functional groups such as pyridine nitrogen, pyrrole nitrogen, and graphite nitrogen. However, some studies have found that only pyridine nitrogen and pyrrole nitrogen are the actual active sites for catalysis. Therefore, it is important to investigate the real active sites and formulate precise synthetic methods before doping. In addition, some codoping strategies have achieved remarkable results, which encourage researchers to invest more efforts in exploring the synergistic effects of heteroatoms in the future.

4.3.2. Vacancy Engineering

Vacancy engineering is regarded as another important strategy to adjust the physical or chemical properties of materials. It has been proven that the introduction of vacancies can tune the electronic structure, increase the electron trapping capacity, and improve the surface adsorption capacity. In addition, vacancies with plenty of localized electrons are also good anchoring sites for single atoms (SAs). Vacancy can be simply divided into anion vacancies and cation vacancies according to their different oxidation states. Anion vacancies, such as oxygen vacancies,^[179] sulfur vacancies,^[180] and nitrogen vacancies,^[181] have been widely studied because of their low formation energy, while cation vacancies have not been paid much attention because of their higher formation energy barriers relative to anion vacancies. At present, in addition to the doping process described in the previous section that can create vacancies, other effective methods, such as heat treatment in an oxygen-deficient environment,^[182] chemical reduction,^[183] and plasma treatment have also been developed.^[184]

Oxygen vacancy (V_o) has been widely studied due to its low formation energy. Previous studies have shown that the V_os on the surface of metal oxides are the active centers for N₂ adsorption and activation. Very recently, Ye and co-workers found that In₂O_{3-x}/CeO_{2-y} with V_os can stretch the N≡N adsorbed on its surface through DFT calculations, which would lower the energy barrier and benefit the NRR reaction.^[185] They prepared In₂O_{3-x}/CeO_{2-y} nanotubes (In₂-Ce₁, In₁-Ce₁, In₁-Ce₂) as NRR catalysts with different In/Ce ratios (2:1, 1:1, 1:2) by electrospinning (Figure 11a). In₁-Ce₁ had the highest specific surface area, the largest electrochemical active surface area (ECSA), and the smallest charge transfer resistance, which were beneficial to expose more active sites and increase the selectivity of NRR. As shown in Figure 11b,c, both EPR spectrum and Fourier transform extended X-ray absorption fine structure (EXAFS) spectrum confirmed the existence of V_os of In₁-Ce₁. The well-designed In₁-Ce₁ exhibited the highest NH₃ yield of 26.1 μg h⁻¹ mg⁻¹_{cat.} and the maximum FE of 16.1% at -0.3 V versus RHE.

In addition, Liu and co-workers have designed several V_o-rich spinel nanosheets loaded on hollow nitrogen-doped carbon polyhedra (HNCP) under the guidance of DFT calculations.^[186] Taking V_o-rich NiCo₂O₄ on HNCP (V_o-rich NiCo₂O₄@HNCP) as

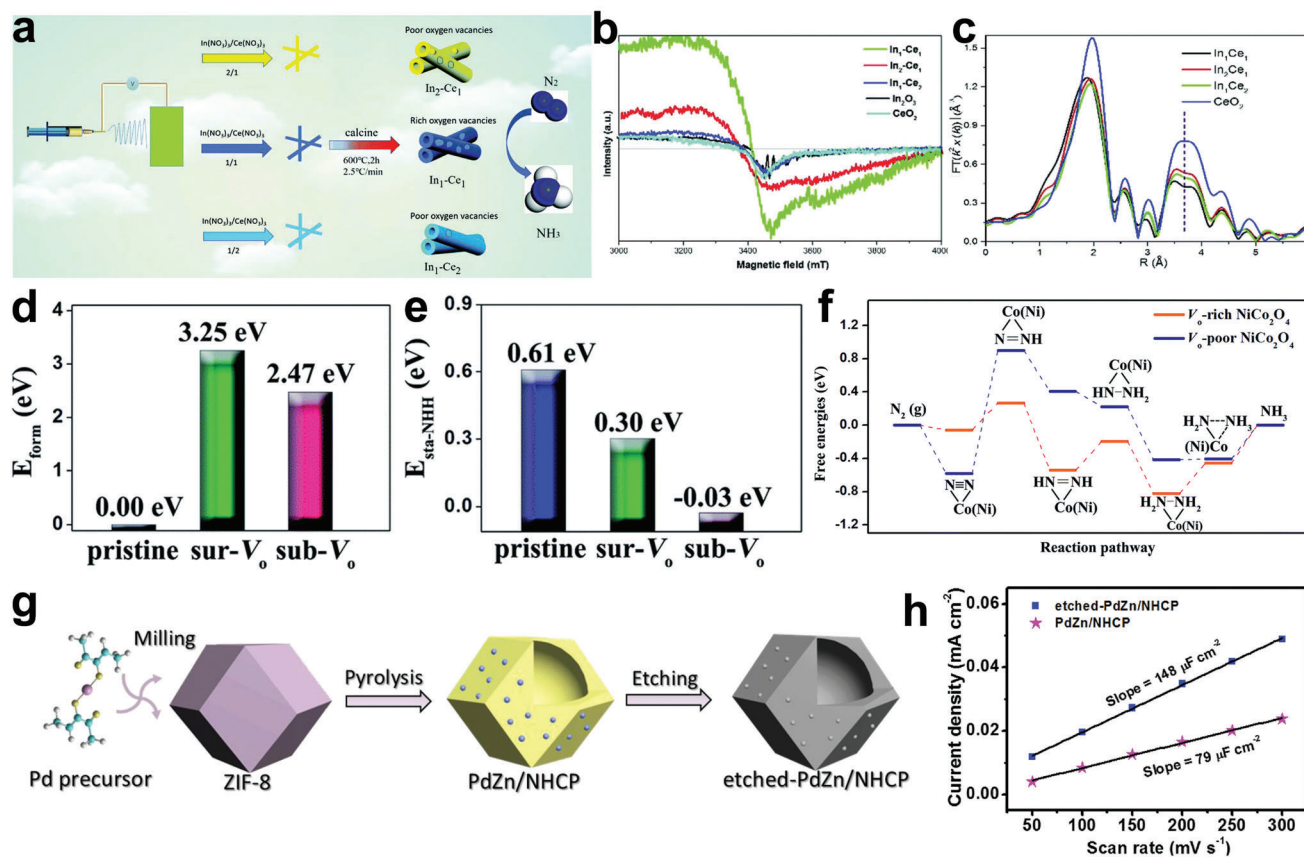


Figure 11. a) Schematic illustration of the formation of the V_o -rich In_2O_{3-x}/CeO_{2-y} . b) EPR spectra of the different catalysts. c) EXAFS signals in R-space of the catalysts. Reproduced with permission.^[185] Copyright 2020, Royal Society of Chemistry. d) Formation energy of oxygen vacancy for different catalyst models. e) Adsorption energy of NNH groups in different catalyst models. f) Free energy diagram of V_o -rich $NiCo_2O_4$ @HNCP. Reproduced with permission.^[186] Copyright 2020, Royal Society of Chemistry. g) Schematic diagram of the formation process of etched-PdZn/NHCP. h) Capacitive currents versus scan rates for different catalysts. Reproduced with permission.^[188] Copyright 2020, Elsevier.

an example, both XPS and X-ray absorption near edge structure spectra confirmed the existence of abundant V_o s. In addition, they found that the annealing temperature would affect the content of V_o s. The type of V_o was also an important factor in determining the catalytic activity. There were two types of oxygen, surface oxygen and subsurface oxygen, in the perfectly crystallized $NiCo_2O_4$ lattice. As shown in Figure 11d,e, subsurface oxygen vacancy (sub- V_o) had lower formation energy and higher adsorption capacity for NNH groups. In 0.1 M Na_2SO_4 , the best NRR performance of V_o -rich $NiCo_2O_4$ @HNCP (NH_3 yield: $4.1 \mu g h^{-1} cm^{-2}$; FE: 5.3%) was obtained at -0.25 V versus RHE, which was better than V_o -rich $NiCo_2O_4$ bulk and V_o -poor $NiCo_2O_4$ @HNCP (V_o -poor $NiCo_2O_4$ @HNCP). Furthermore, theoretical calculations indicated that the NRR process on the catalyst surface may follow an associative alternating pathway. In comparison to V_o -poor $NiCo_2O_4$ @HNCP, V_o -rich $NiCo_2O_4$ @HNCP had lower free energy, suggesting that introducing vacancies was indeed beneficial to the NRR process (Figure 11f). The well-designed V_o s and hollow structures synergistically promoted the catalytic performance, as also confirmed in other spinel hollow structural materials ($ZnCo_2O_4$ @HNCP and Co_3O_4 @HNCP).

The presence of anion vacancies can effectively improve the NRR catalytic activity of catalysts, which motivates researchers to

further explore cation vacancies. Wang and co-workers prepared MoN nanocrystals with rich Mo vacancies anchored on N-doped carbon (MV-MoN@NC) through utilizing SiO_2 spheres as templates and etching treatment.^[187] In HRTEM image, a myriad of defects were found in MV-MoN@NC, which was subsequently confirmed by EPR and XPS spectra. In addition, MV-MoN@NC had the highest ECSA value and the best charge transfer ability, which indicated that Mo vacancy not only improved the catalytic activity but also enhanced the electrical conductivity. The hollow structure and vacancies synergistically worked on the cleverly designed MV-MoN@NC, showing much higher NH_3 yield ($76.9 \mu g h^{-1} mg^{-1}_{cat}$) than MoN@NC ($31.1 \mu g h^{-1} mg^{-1}_{cat}$), MoN ($9.2 \mu g h^{-1} mg^{-1}_{cat}$), and NC ($2.2 \mu g h^{-1} mg^{-1}_{cat}$). The ^{15}N isotope tracer experiment and DFT calculation confirmed that the reaction pathway of MV-MoN@NC was the MvK pathway.

Kuang and co-workers prepared PdZn nanoparticles loaded on nitrogen-doped hollow carbon polyhedrons (etched-PdZn/NHCP) by pyrolyzing the MOF precursors and etching strategy (Figure 11g).^[188] Various characterization methods such as HRTEM, XPS, and EPR confirmed that the etched-PdZn/NHCP contained a myriad of Zn vacancies, which would facilitate the capture and further activation of N_2 . The etching process not only removed ZnO nanoparticles in the material, but

also increased the specific surface area of the material. Moreover, the ECSA of the material was also enhanced by etching, which was more conducive to the NRR reaction (Figure 11h). The synergistic effect of etching PdZn and NHCP with a large number of vacancies resulted in a remarkable FE of 16.9% and an NH_3 yield of $5.28 \mu\text{g h}^{-1} \text{mg}^{-1}_{\text{cat}}$ at -0.2 V versus RHE, far better than that of PdZn/NHCP ($3.18 \mu\text{g h}^{-1} \text{mg}^{-1}_{\text{cat}}$), commercial Pd/C ($1.52 \mu\text{g h}^{-1} \text{mg}^{-1}_{\text{cat}}$), and pure ZIF-8-derived N-doped carbon ($0.68 \mu\text{g h}^{-1} \text{mg}^{-1}_{\text{cat}}$) under the same test conditions. The excellent performance of the designed catalyst was attributed to the following factors: the hollow structure that promoted electrolyte penetration and supported Pd/Zn nanoparticles, N-doped carbon that improved the electron transfer rate, and defects that induced local electron-rich activation of N_2 after etching.

In conclusion, vacancy engineering is of great significance for improving the catalytic activity by improving the conductivity, regulating the electronic structures, and optimizing the active sites of catalysts. However, there are still some challenges that hinder the further development of vacancy engineering. 1) At present, most of the studies focus on the oxygen vacancies and nitrogen vacancies of anion vacancies, while other types of anion vacancies are not well explored. Similarly, from the effective improvement of electronic structure caused by anionic vacancies, it can be inferred that cationic vacancies are also promising alternative strategies that deserve extensive exploration. At the same time, combining multiple vacancies in the same catalyst is also a possible way to synergistically improve the catalytic performance due to differences in electronegativity and atomic radius. 2) The intrinsic relationship between vacancy content and catalytic activity is still unclear, so it is necessary to measure the vacancy contents correctly. At present, XPS is commonly used to identify the vacancy contents. However, XPS is a surface characterization method, and the fact that fitting of the vacancy contents is subjective makes it difficult to accurately reveal the actual contents of vacancy. Scanning tunneling microscope can intuitively observe the existence of vacancies, but it can only be used in a small area and cannot comprehensively count the vacancy contents. Therefore, it is necessary to develop advanced characterization techniques to determine the type and vacancy concentrations. 3) Last but not the least, in order to maintain the durability of the catalyst, the vacancies as active sites should stay stable for a long term, therefore, the stability of vacancies should be also considered when manufacturing defective catalysts.

4.3.3. Single Atom Engineering

Recently, scientists have developed atomic-scale dispersed single atomic catalysts (SACs).^[189,190] Atom-level exposure of SACs makes full use of individual atoms, not only improving quality and yield, but also effectively saving costs, especially for precious metals. At present, SACs have made considerable progress in the field of catalysis, such as oxygen reduction reaction,^[191] carbon dioxide reduction reaction,^[192] oxygen evolution reaction,^[193] HER,^[194] and NRR.^[195] However, their surface energy is high due to the reduced size, making it necessary to find a suitable substrate to anchor them. Carbon-based materials with high conductivity and large specific surface area are widely used as carriers for

SACs. Among them, carriers with hollow characteristics such as CNTs and MOF derivatives are favored.^[196,197]

Fe-N_3 is considered to be a potent active site for NRR. As a proof-of-concept experiment, Cui and co-workers synthesized Fe-N/C-CNTs as NRR catalysts by pyrolyzing the iron-doped ZIF-8 dispersed on CNTs (Figure 12a).^[197] Fe SAs played a decisive role for enhancing NRR performance, which was confirmed by N_2 -TPD. The results showed that Fe-N/C-CNTs not only obtained enhanced physical adsorption capacity, but also achieved superior nitrogen chemical adsorption capacity, which confirmed the excellent binding force of N_2 and Fe SAs. In addition, ZIF-8 crystals were uniformly loaded on the surface of CNTs, which resulted in a high specific surface area of Fe-N/C-CNTs and effectively increased the catalytic active area. At -0.2 V versus RHE, the ingeniously designed Fe-N/C-CNTs showed the highest NH_3 yield of $34.83 \mu\text{g h}^{-1} \text{mg}^{-1}_{\text{cat}}$ and the corresponding FE of 9.28%, which were higher than N-doped carbon on CNTs (NC-CNTs) and CNTs. Fe-N/C-CNTs were deactivated by SCN^- toxicity under acidic conditions and reactivated by dissociation of SCN^- under alkaline conditions, which agreed with the hypothesis that Fe-N₃ was the active site of NRR. Furthermore, the NH_3 yield depended on not only the iron content, but also the pyridine nitrogen content, which indicated that the pyridine nitrogen was the anchor point of Fe-N₃ (Figure 12b). SAs are known as ideal N_2 adsorption sites, so more other kinds of SAs based on hollow structural materials should be manufactured. The development of SA anchor sites is another priority, for it is not only a prerequisite for SAs' stability but also a determining factor of SAs' total number.

Meanwhile, SAs can also synergize with nanoparticles to promote NRR. The theoretical study of Wang and co-workers showed that Mo_2C and MoSAs exhibited the selectivity of HER and NRR, respectively.^[198] Accordingly, Mo_2C was expected to obtain a large amount of *H provided by MoSAs to activate N_2 , which would enable the catalyst complex combining Mo_2C and MoSAs to improve selectivity and activity at the same time. Subsequently, MoSAs and Mo_2C were assembled into N-doped carbon nanotubes (MoSAs- $\text{Mo}_2\text{C}/\text{NCNTs}$) as NRR cathode materials. MoSAs- $\text{Mo}_2\text{C}/\text{NCNTs}$ exhibited the highest NH_3 yield of $16.1 \mu\text{g h}^{-1} \text{cm}_{\text{cat}}^{-2}$ and the maximum FE of 7.1%, which were better than the single component MoSAs/NCNTs ($3.3 \mu\text{g h}^{-1} \text{cm}_{\text{cat}}^{-2}$, 1.4%) and $\text{Mo}_2\text{C}/\text{NCNTs}$ ($4.3 \mu\text{g h}^{-1} \text{cm}_{\text{cat}}^{-2}$, 3.6%). Although the synergy is proposed by combining the experimental results with the modeling calculations, the conclusion derivation process is often not comprehensive enough, which calls for the utilization and advancement of in situ characterization methods (such as in situ X-ray absorption spectroscopy, in situ microscopy, etc.).

In addition to single metal SAs, as shown in Figure 12c, Liang and co-workers used C_3N_4 supported on CNT to anchor Fe and Cu SAs (CNT@ C_3N_4 -FeandCu) as an efficient NRR catalyst.^[199] Scanning transmission electron microscopy (STEM) confirmed that the surface of the material contained a large number of SAs with most of them being in a triplet state (Figure 12d). The distance between SAs in the triplet state was 1.8–2.5 Å, very close to the bond length of $\text{N}\equiv\text{N}$. Such distance was enough to produce a synergistic effect between SAs as supported by the theoretical calculations.^[200] When a N_2 is adsorbed on an active site with three metal atoms, the three metal atoms can stabilize N_2 at the same time, which can avoid the formation of strong N-metal

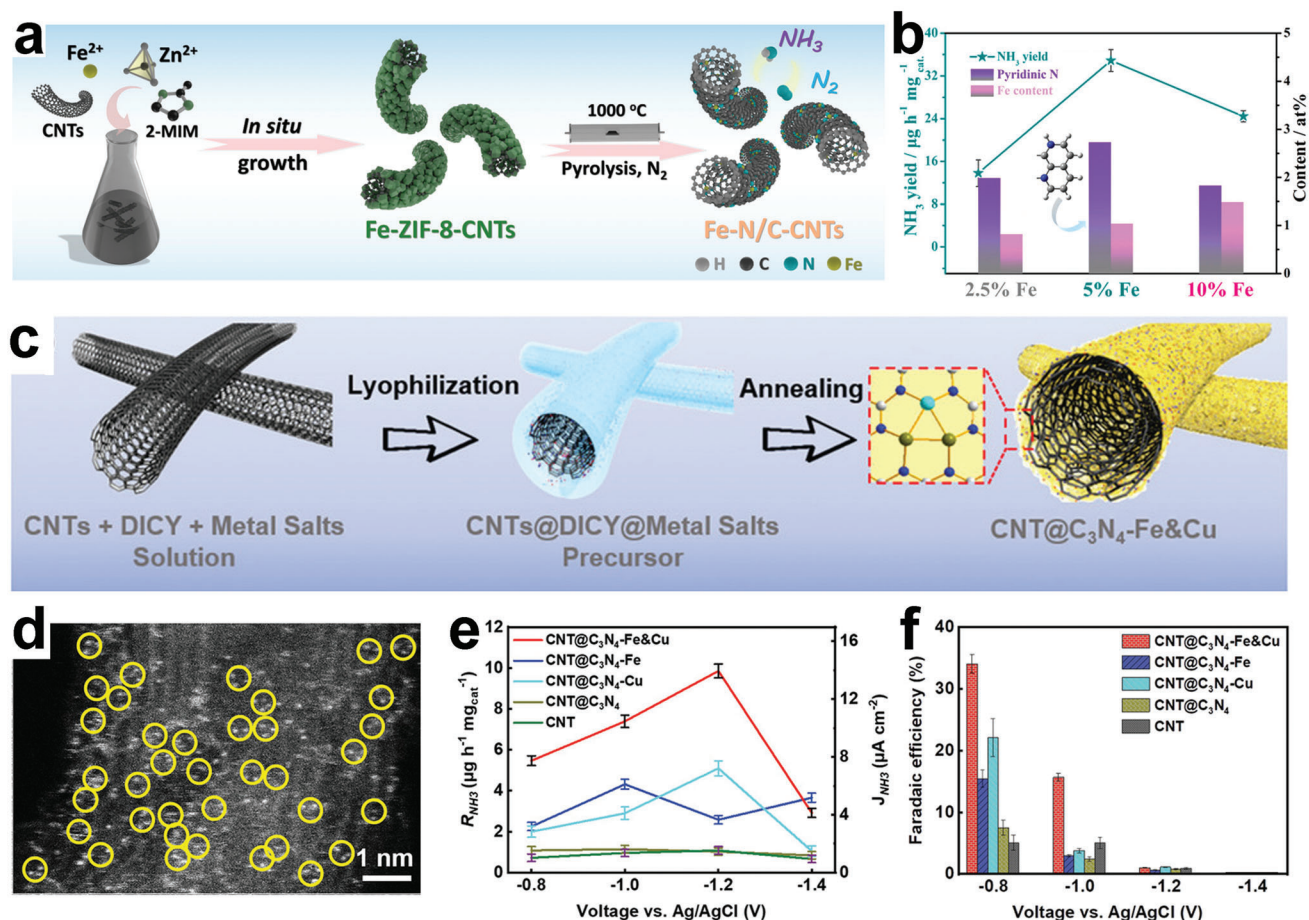


Figure 12. a) Scheme illustration of the synthesis of Fe-N/C-CNTs. b) Correlation between NH₃ yields and different N contents of Fe-N/C-CNTs with different amounts of Fe. Reproduced with permission.^[197] Copyright 2019, American Chemical Society. c) Schematic illustration of preparation and morphology of CNT@C₃N₄-Fe&Cu. d) STEM image of CNT@C₃N₄-Fe&Cu. e) NH₃ yields and partial current densities of different catalysts. f) FE of different catalysts. Reproduced with permission.^[199] Copyright 2020, Wiley-VCH.

bonds, thereby realizing low-energy NH₃ desorption. As shown in Figure 12e,f, the as-prepared CNT@C₃N₄-Fe&Cu obtained the best NH₃ yield of 10.27 µg h⁻¹ mg⁻¹ cat. and an excellent FE of up to 34%, which were better than Fe or Cu SAs analogues (CNT@C₃N₄-Fe and CNT@C₃N₄-Cu). The DFT calculations showed that the PDS of CNT@C₃N₄-Fe&Cu (*N₂ → *N₂H, ΔG = 0.58 eV) was better than that of CNT@C₃N₄-Fe (*NH → *NH₂, ΔG = 0.71 eV) and CNT@C₃N₄-Cu (N₂ → *N₂, ΔG = 0.86 eV). This bimetallic SAs with triplet state enhanced the adsorption of N₂ and achieved a reaction process with a lower energy barrier, which is of great significance for low-cost NH₃ production under mild conditions.

In short, SAs are considered to be good NRR catalyst candidates due to their unique electronic structure, uniform low-coordination environment, and atomically dispersed active sites, which can maximize the exposure of active sites. Anchoring SAs on the surface of hollow structural materials through strong coordination can effectively prevent their agglomeration, so as to efficiently and stably catalyze the conversion of N₂ to NH₃. Such excellent catalytic performance has led researchers to develop SACs with higher loading amounts. However, it is important to note that improving the anchor point of SAs is a prerequisite and the

synergistic effect of SAs and other active components is worth further investigation.

4.3.4. Other Engineering

Amorphous materials have a disordered arrangement of atoms and highly unsaturated coordination sites, which will produce dangling bonds, introduce a large number of defects, and effectively enhance catalytic activity.^[201,202] As shown in Figure 13a, Yu and co-workers prepared a Bi₄V₂O₁₁/CeO₂ composite (BVC-A) with an amorphous phase by electrospinning.^[203] They found that CeO₂ could hinder heat transfer, and by adjusting the ratio of Ce to Bi, it might be possible to produce materials with different crystal shapes. When Ce:Bi was 1:2, a hollow amorphous Bi₄V₂O₁₁ nanofiber and CeO₂ nanocrystal hybrid (BVC-A) were produced, while when Ce:Bi was 1:4, a Bi₄V₂O₁₁ nanocrystal and CeO₂ nanocrystal hybrid (BVC-C) were produced. As shown in Figure 13b,c, XPS spectroscopy demonstrated that amorphization could also induce oxygen vacancies in addition to introducing tetravalent defects V. In addition, CeO₂ would also form a heterojunction with amorphous Bi₄V₂O₁₁, as shown in

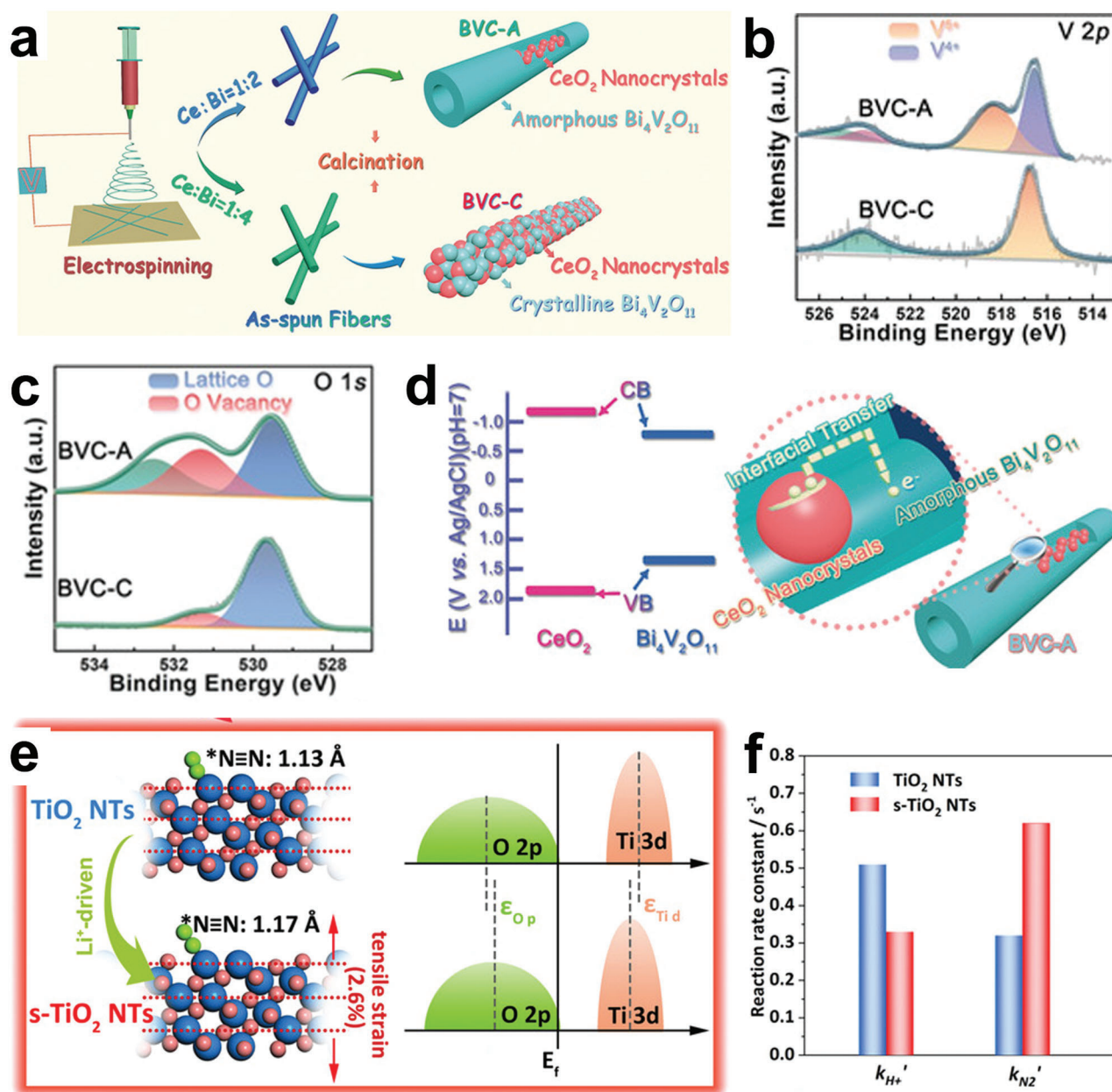


Figure 13. a) Schematic illustration of the preparation of BVC-A and BVC-C electrocatalysts. b) XPS spectra of V 2p. c) XPS spectra of O 1s. d) Band alignment of CeO_2 and $\text{Bi}_4\text{V}_2\text{O}_{11}$ and scheme of interfacial charge transfer of BVC-A. Reproduced with permission.^[203] Copyright 2018, Wiley-VCH. e) Bond length of adsorbed N_2 on different catalysts and the relative density of states. f) Reaction rate constants of H^+ and N_2 adsorption on Ti^{3+} site in different catalysts. Reproduced with permission.^[28] Copyright 2020, Wiley-VCH.

Figure 13d. The resulting $\text{Bi}_4\text{V}_2\text{O}_{11}/\text{CeO}_2$ composite displayed a type I band alignment, which would facilitate the electron transfer from CeO_2 to $\text{Bi}_4\text{V}_2\text{O}_{11}$. BVC-A displayed the optimum NH_3 production rate of $23.21 \mu\text{g h}^{-1} \text{mg}^{-1}_{\text{cat}}$ and the highest FE of 10.16% at -0.2 V versus RHE. BVC-A obtained more excellent NRR activity than BVC-C and pure CeO_2 and $\text{Bi}_4\text{V}_2\text{O}_{11}$, thanks to a multitude of defect sites from the amorphousness, the large active surface area exposed by the hollow structure, and the acceleration of electron transport by heterostructure.

Lattice strain is a strategy to change the surface electronic structure and affect the catalytic activity by adjusting the distance between surface atoms.^[204,205] Yu and co-workers investigated the influence of morphology on catalytic performance and found that the tubular materials can effectively increase the yield because they have both the high selectivity and high surface area of annular surfaces.^[28] Furthermore, the theoretical calculations found that the Li^+ intercalation and deintercalation were able to stretch the $\text{N}\equiv\text{N}$ of N_2 adsorbed on Ti^{3+} sites and reduce the

formation energy of oxygen vacancies for further stabilizing Ti^{3+} , as shown in Figure 13e. Through theoretical inferences, they prepared lattice-strained TiO_2 nanotubes (s- TiO_2 NTs) by utilizing electrochemical Li^+ intercalation and deintercalation strategies. The reaction rate constants of N_2 and H^+ adsorbed on s- TiO_2 NTs and TiO_2 NTs were measured by in situ surface interrogation scanning electrochemical microscopy technique, indicating the higher NRR selectivity of N_2 and H^+ adsorbed on s- TiO_2 NTs (Figure 13f). The NH_3 yield ($16.67 \mu g h^{-1} mg^{-1}_{cat.}$) and FE (26%) of the elaborately prepared s- TiO_2 NTs showed a substantial increase compared to TiO_2 NTs and TiO_2 thin films. DFT calculations revealed that s- TiO_2 NTs were more conducive to N_2 adsorption, so they were first protonated at lower energy as a rate-determining step, and then NRR is effectively performed along the associative distal pathway. This interesting work encourages researchers to investigate the effects of metal ion intercalation and deintercalation strategies on lattice strain. In short, amorphous and lattice strains are effective strategies for optimizing hollow structural catalysts and deserve in-depth study.

5. Summary and Outlook

The electrocatalytic conversion of N_2 to NH_3 under environmental conditions has become an attractive subject in line with the background of carbon neutral. As promising catalysts, the hollow structural materials have fascinating merits, including large specific surface area, high atomic utilization, reliable structural stability, low mass and charge transfer pathway, and the confined cavity on reactants, which make them to be excellent candidates for NRR electrocatalysts. In this review, the latest research progress of NRR hollow structural electrocatalysts under mild circumstances from intrinsic, mesoscopic to microscopic regulations is reviewed (Table 1). Here, the main challenges faced in pursuit of obtaining extraordinary and efficient hollow structural electrocatalysts that can meet the requirements of industrial grades are summarized.

i) Hollow structural catalyst synthesis: Hollow materials with different structural features are usually synthesized by hard template, soft template, and self-template/template-free methods, each of which has its own advantages and disadvantages. However, there is still a long way to go to obtain the hollow materials with precise and controllable structures. Here, the following suggestions are proposed in order to develop a “green” synthetic method. 1) Factors such as cost saving, environment-friendly, and large-scale production should be considered in the process of developing new strategies to achieve industrial applications instead of being limited to laboratory research; meanwhile, the synthetic methods of using highly corrosive and toxic chemicals should be optimized. 2) It is meaningful to control the exposure number of active spots in hollow structural materials because that the number of active sites is generally proportional to the catalytic activity. Therefore, the size, morphology, pore structure, and shell thickness of the hollow structural material should be properly regulated to capture reactants and activate nitrogen molecules. 3) The synthesis of hollow structure models that can define active components is conducive to clarifying the reaction mechanism, and has profound guiding significance for future design and synthesis.

ii) Intrinsic regulation of hollow structural catalysts: High specific surface area and abundant cavities of the intrinsic hollow structural material provide highly unsaturated coordination and highly accessible surface sites for the catalytic reaction, guaranteeing high apparent activity. It is worth noting that the inner surface of the hollow structural material is less affected by the capping agent, so it may exhibit higher catalytic activity than the outer surface. Abundant cavities can limit diffusion of reaction intermediates and increase their collision possibility, thus increasing the probability of being captured by active sites. In addition, the stability of the hollow structures can prevent the aggregation and deactivation of active sites, making the catalysts more durable. These unique advantages promise the hollow structural materials to be strong candidates for NRR catalysts. Nevertheless, in order to obtain better catalytic activity, the shell thickness and pore size of hollow structural materials should be carefully designed. The thinner the shell thickness, the greater the atomic utilization and the larger the specific surface area, with the structural stability being well retained. The extreme small pore size would hinder the diffusion of the reactants, while large pore size would diminish specific surface area and also make it difficult to restrict the reactants.

iii) Mesoscopic regulation of hollow structural catalysts: From the mesoscopic point of view, the hollow structural materials could be used as good carriers due to their highly unsaturated coordination sites and reliable structural stability, which can increase N_2 adsorption sites by anchoring other components. First of all, the hollow structural materials can uniformly scatter nanoparticles or other molecules, and in this way, the supported components can be prevented from agglomerating during catalysis, thereby improving the durability of the catalysts. Second, the hollow structural materials are capable of constructing heterostructures with other components and forming heterogeneous interfaces, which are conducive to enhancing the conductivity, promoting the adsorption of reactants, and accelerating the interfacial electron transfer. Third, some unstable active ingredients can improve their stability by forming core-shell heterostructures. Although in most cases mesoscopically regulated hollow structural materials are used as carriers, the activity of the hollow structural materials themselves should not be ignored. The performance of catalysts is not simply superimposed by hollow structural materials and other components, so we should not just summarize the active ingredients from synergistic effects without giving detailed evidence. Therefore, it is necessary to design control experiments ingeniously based on the advanced theoretical calculations to further distinguish their respective contributions.

iv) Microscopic regulation of hollow structural catalysts: From the microscopic point of view, the local coordination environment of hollow structural materials can be adjusted through the modification of atomic structures to improve catalytic activity. The strategy of introducing heteroatoms through doping could redistribute the electron density of the structures, thereby forming surface defects to improve the binding ability with N_2 . The fabrication of vacancies could increase the conductivity, tune the electronic structure, and optimize the active sites. The hollow structural material used to anchor SAs can not only increase the active sites, but also form electronic interactions generated by metal-substrate coordination that often produce impressive

Table 1. A summary of reported hollow structural materials as NRR electrocatalysts in recent years and their catalytic performance.

	Catalyst	Electrolyte	NH ₃ yield rate	Faradaic efficiency [%]	Potential ([V] vs RHE)	Ref.
Intrinsic	VO ₂ microspheres	0.1 M Na ₂ SO ₄	14.85 μg h ⁻¹ mg ⁻¹ _{cat.}	3.97	-0.7	[128]
	Bi ₂ MoO ₆ spheres	0.1 M HCl	20.46 μg h ⁻¹ mg ⁻¹ _{cat.}	8.17	-0.6	[129]
	Bi nanospheres	0.1 M Na ₂ SO ₄	23.4 ± 1.3 μg h ⁻¹ mg ⁻¹ _{cat.}	19.8 ± 1.1	-0.4	[130]
	Cr ₂ O ₃ microspheres	0.1 M Na ₂ SO ₄	25.3 μg h ⁻¹ mg ⁻¹ _{cat.}	6.78	-0.9	[131]
	MoPi microspheres	0.1 M KOH	18.66 μg h ⁻¹ mg ⁻¹ _{cat.}	9.04	-0.2	[135]
	CoPi microspheres	0.1 M KOH	16.48 μg h ⁻¹ mg ⁻¹ _{cat.}	4.46	-0.2	[136]
	CoPc nanotubes	0.1 M HCl	107.9 μg h ⁻¹ mg ⁻¹ _{cat.}	27.7	-0.3	[137]
	Au nanocages	0.5 M LiClO ₄	3.9 μg cm ⁻² h ⁻¹	30.2	-0.5, -0.4	[31]
	Au nanocage-715	0.5 M LiClO ₄	3.74 μg cm ⁻² h ⁻¹	35.9	-0.4	[138]
	CrN nanocube	0.1 M HCl	31.11 μg h ⁻¹ mg ⁻¹ _{cat.}	16.6	-0.5	[206]
Mesoscopic	FePc/O-MWCNT	0.1 M HCl	36 μg h ⁻¹ mg ⁻¹ _{cat.}	9.73	-0.3	[144]
	NCNT/Fe ₃ C	0.1 M KOH	15.508 μg h ⁻¹ mg ⁻¹ _{cat.}	2.72	-0.4	[145]
	CuCo ₂ S ₄ /MWCNT	0.1 M Na ₂ SO ₄	137.5 μg h ⁻¹ mg ⁻¹ _{cat.}	8.7	-0.5	[146]
	Ru-PEI@MWCNTs	0.1 M KOH	188.9 μg h ⁻¹ mg ⁻¹ _{cat.}	30.93	-0.1	[147]
	Mn ₃ O ₄ /b-TiO ₂	0.1 M KOH	1.61 × 10 ⁻¹⁰ mol s ⁻¹ cm ⁻²	25.2	-0.45, -0.35	[148]
	BP@SnO _{2-x}	0.1 M Na ₂ SO ₄	48.87 μg h ⁻¹ mg ⁻¹ _{cat.}	14.6	-0.4	[149]
	NiCoS/C	0.1 M Li ₂ SO ₄	58.5 μg h ⁻¹ mg ⁻¹ _{cat.}	12.9	-0.2, 0	[161]
	CoVP@NiFeV-LDHs	0.05 M H ₂ SO ₄	27.2 μg h ⁻¹ mg ⁻¹ _{cat.}	13.8	-0.3	[162]
	Ni@NCNTs	0.1 M HCl	53.88 μg h ⁻¹ mg ⁻¹ _{cat.}	7.3	-0.5, -0.3	[163]
	PdO/Pd/CNTs	0.1 M NaOH	18.2 μg h ⁻¹ mg ⁻¹ _{cat.}	11.5	0, 0.1	[164]
	C@NiO@Ni	0.1 M KOH	43.15 μg h ⁻¹ mg ⁻¹ _{cat.}	10.9	-0.7	[165]
	Au ₃ Cu@Cu	0.1 M Na ₂ SO ₄	33.97 μg h ⁻¹ mg ⁻¹ _{cat.}	21.41	-0.2	[167]
	Co ₃ O ₄ @NCs	0.05 M H ₂ SO ₄	42.58 μg h ⁻¹ mg ⁻¹ _{cat.}	8.5	-0.2	[166]
	Au-Ag-Pd-850	0.5 M LiClO ₄	13.74 μg h ⁻¹ mg ⁻¹ _{cat.}	48.94	-0.3	[207]
	Co-MoS ₂ /N@C	0.1 M Na ₂ SO ₄	129.93 μg h ⁻¹ mg ⁻¹ _{cat.}	11.21	-0.4	[208]
	1T'-MoS ₂ /TiO ₂	0.1 M Na ₂ SO ₄	29.62 μg h ⁻¹ mg ⁻¹ _{cat.}	24.9	-0.75, -0.65	[209]
	Microscopic	S-CNS	0.1 M Na ₂ SO ₄	19.07 μg h ⁻¹ mg ⁻¹ _{cat.}	7.47	-0.7
O-C microtubes		0.1 M HCl	25.12 μg h ⁻¹ mg ⁻¹ _{cat.}	9.1	-0.85, -0.80	[210]
O-CNT		0.1 M LiClO ₄	32.33 μg h ⁻¹ mg ⁻¹ _{cat.}	12.50	-0.4	[211]
P-CNTs		0.25 M LiClO ₄	24.4 μg h ⁻¹ mg ⁻¹ _{cat.}	12.5	-1.1, -0.3	[172]
Fe-TiO ₂		0.1 M Na ₂ SO ₄	43.14 μg h ⁻¹ mg ⁻¹ _{cat.}	16.35	-0.7	[174]
Zr-TiO ₂		0.1 M KOH	8.90 μg h ⁻¹ mg ⁻¹ _{cat.}	17.3	-0.45	[175]
Pt-FeP/C		0.1 M KOH	54.75 μg h ⁻¹ mg ⁻¹ _{cat.}	15.3	-0.1, -0.05	[177]
Fe,Mo-N/C		0.1 M Na ₂ SO ₄	38.76 μg h ⁻¹ mg ⁻¹ _{cat.}	14.2	-0.1	[176]
NiFe-MoS ₂		0.1 M Na ₂ SO ₄	106.59 μg h ⁻¹ mg ⁻¹ _{cat.}	7.15	-0.3, -0.2	[178]
In ₂ O _{3-x} /CeO _{2-y}		0.1 M KOH	26.1 μg h ⁻¹ mg ⁻¹ _{cat.}	16.1	-0.3	[185]
NiCo ₂ O ₄ @HNCP		0.1 M Na ₂ SO ₄	17.8 μg h ⁻¹ mg ⁻¹ _{cat.}	5.3	-0.25	[186]
MV-MoN@NC		0.1 M HCl	76.9 μg h ⁻¹ mg ⁻¹ _{cat.}	6.9	-0.2	[187]
etched-PdZn/NHCP		0.1 M phosphate-buffered saline	5.28 μg h ⁻¹ mg ⁻¹ _{cat.}	16.9	-0.2	[188]
Fe-N/C-CNTs		0.1 M KOH	34.83 μg h ⁻¹ mg ⁻¹ _{cat.}	9.28	-0.2	[197]
MoSAs-Mo ₂ C/NCNTs		0.005 M H ₂ SO ₄ + 0.1 M K ₂ SO ₄	16.1 μg h ⁻¹ mg ⁻¹ _{cat.}	7.1	-0.25, -0.2	[198]
CNT@C ₃ N ₄ -FeandCu		0.25 M LiClO ₄	10.27 μg h ⁻¹ mg ⁻¹ _{cat.}	34	-1.2, -0.8	[199]
Bi ₄ O ₁₁ /CeO ₂		0.1 M HCl	23.21 μg h ⁻¹ mg ⁻¹ _{cat.}	10.16	-0.2	[203]
s-TiO ₂		0.1 M HCl	16.67 μg h ⁻¹ mg ⁻¹ _{cat.}	26	-0.6, -0.45	[28]
CoP		1.0 M KOH	10.78 μg h ⁻¹ mg ⁻¹ _{cat.}	7.36	-0.4, 0	[212]
C@CoFe ₂ O _{4-x}	0.1 M Na ₂ SO ₄	30.97 μg h ⁻¹ mg ⁻¹ _{cat.}	11.65	-0.4	[213]	

catalytic performance. In addition, amorphous and lattice strains, which have not been widely concerned, are also effective strategies for adjusting hollow structural materials. Although many microscopic regulation strategies have been developed that can effectively improve the catalytic performance of hollow structural catalysts, there are still problems in various strategies, such as the precise regulation of defect concentrations, and the precise synthesis in specific coordination environments. Meanwhile, the internal mechanism of various strategies to promote the efficient implementation of NRR is still unclear. In conclusion, there is an urgent need to develop microscopic regulation strategies with universality and controllability, and to further explore their respective roles in the catalytic process by combining advanced characterization techniques with theoretical calculations.

In short, hollow structural materials are excellent electrocatalysts for the conversion of N_2 to NH_3 under environmental conditions. In this review, the latest developments in the hollow structural catalysts have been reviewed, focusing on synthetic methods and regulating strategies. In order to design the catalyst more rationally, suggestions for optimizing synthetic methods and a top-down fine regulating strategy have been proposed. It is anticipated to obtain more active, selective and stable hollow structural catalysts for the efficient production of NH_3 in the future and even for industrial applications.

Acknowledgements

This work was supported by the National Natural Science Foundation (Grant Nos. 22075133, 21727808, 21971114, and 21701086), the National Science Funds for Distinguished Young Scholars (Grant No. 21625401), and the Jiangsu Provincial Funds for Natural Science Foundation (Grant No. BK20200090).

Conflict of Interest

The authors declare no conflict of interest.

Keywords

electrocatalysis, hollow structural materials, nitrogen reduction reaction, regulation strategies, synthetic methods

Received: September 19, 2021

Revised: October 21, 2021

Published online: December 10, 2021

- [1] J. G. Chen, R. M. Crooks, L. C. Seefeldt, K. L. Bren, R. M. Bullock, M. Y. Darensbourg, P. L. Holland, B. Hoffman, M. J. Janik, A. K. Jones, M. G. Kanatzidis, P. King, K. M. Lancaster, S. V. Lymar, P. Pfromm, W. F. Schneider, R. R. Schrock, *Science* **2018**, *360*, eaar6611.
- [2] B. H. R. Suryanto, K. Matuszek, J. Choi, R. Y. Hodgetts, H.-L. Du, J. M. Bakker, C. S. M. Kang, P. V. Cherepanov, A. N. Simonov, D. R. MacFarlane, *Science* **2021**, *372*, 1187.
- [3] R. F. Service, *Science* **2018**, *361*, 120.
- [4] O. Elishav, B. Mosevitzky Lis, E. M. Miller, D. J. Arent, A. Valera-Medina, A. Grinberg Dana, G. E. Shter, G. S. Grader, *Chem. Rev.* **2020**, *120*, 5352.

- [5] C. Tang, S.-Z. Qiao, *Chem. Soc. Rev.* **2019**, *48*, 3166.
- [6] X. Zhao, G. Hu, G.-F. Chen, H. Zhang, S. Zhang, H. Wang, *Adv. Mater.* **2021**, *33*, 2007650.
- [7] B. K. Burgess, D. J. Lowe, *Chem. Rev.* **1996**, *96*, 2983.
- [8] R. D. Milton, S. D. Minteer, *Acc. Chem. Res.* **2019**, *52*, 3351.
- [9] G. N. Schrauzer, T. D. Guth, *J. Am. Chem. Soc.* **1977**, *99*, 7189.
- [10] D. Zhu, L. Zhang, R. E. Ruther, R. J. Hamers, *Nat. Mater.* **2013**, *12*, 836.
- [11] E. E. Van Tamelen, D. A. Seeley, *J. Am. Chem. Soc.* **1969**, *91*, 5194.
- [12] J. Deng, J. A. Iñiguez, C. Liu, *Joule* **2018**, *2*, 846.
- [13] L. Wang, M. Xia, H. Wang, K. Huang, C. Qian, C. T. Maravelias, G. A. Ozin, *Joule* **2018**, *2*, 1055.
- [14] S. L. Foster, S. I. P. Bakovic, R. D. Duda, S. Maheshwari, R. D. Milton, S. D. Minteer, M. J. Janik, J. N. Renner, L. F. Greenlee, *Nat. Catal.* **2018**, *1*, 490.
- [15] J. N. Galloway, E. B. Cowling, *Ambio* **2002**, *31*, 64.
- [16] A. R. Singh, B. A. Rohr, J. A. Schwalbe, M. Cargnello, K. Chan, T. F. Jaramillo, I. Chorkendorff, J. K. Nørskov, *ACS Catal.* **2017**, *7*, 706.
- [17] X. Zhao, Z. Yang, A. V. Kuklin, G. V. Baryshnikov, H. Ågren, W. Liu, H. Zhang, X. Zhou, *ACS Appl. Mater. Interfaces* **2020**, *12*, 31419.
- [18] Y. Gu, B. Xi, W. Tian, H. Zhang, Q. Fu, S. Xiong, *Adv. Mater.* **2021**, *33*, 2100429.
- [19] Y. Tan, L. Yan, C. Huang, W. Zhang, H. Qi, L. Kang, X. Pan, Y. Zhong, Y. Hu, Y. Ding, *Small* **2021**, *17*, 2100372.
- [20] P. Zhang, X. F. Lu, J. Nai, S.-Q. Zang, X. W. Lou, *Adv. Sci.* **2019**, *6*, 1900576.
- [21] J. Yang, L. Yu, B. Zheng, N. Li, J. Xi, X. Qiu, *Adv. Sci.* **2020**, *7*, 1903260.
- [22] I. E. Khalil, C. Xue, W. Liu, X. Li, Y. Shen, S. Li, W. Zhang, F. Huo, *Adv. Funct. Mater.* **2021**, *31*, 2010052.
- [23] C. Yang, Y. Zhu, J. Liu, Y. Qin, H. Wang, H. Liu, Y. Chen, Z. Zhang, W. Hu, *Nano Energy* **2020**, *77*, 105126.
- [24] H. Yu, Z. Wang, S. Yin, C. Li, Y. Xu, X. Li, L. Wang, H. Wang, *ACS Appl. Mater. Interfaces* **2020**, *12*, 436.
- [25] N. C. Kani, A. Prajapati, B. A. Collins, J. D. Goodpaster, M. R. Singh, *ACS Catal.* **2020**, *10*, 14592.
- [26] F. Wang, L. Xia, X. Li, W. Yang, Y. Zhao, J. Mao, *Energy Environ. Mater.* **2021**, *4*, 88.
- [27] W.-J. Liu, G. Yu, M. Zhang, R.-H. Li, L.-Z. Dong, H.-S. Zhao, Y.-J. Chen, Z.-F. Xin, S.-L. Li, Y.-Q. Lan, *Small Methods* **2018**, *2*, 1800154.
- [28] P. Li, Z. Jin, Z. Fang, G. Yu, *Angew. Chem., Int. Ed.* **2020**, *59*, 22610.
- [29] Y. Lv, Y. Wang, M. Yang, Z. Mu, S. Liu, W. Ding, M. Ding, *J. Mater. Chem. A* **2020**, *9*, 1480.
- [30] M. A. Mahmoud, D. O'Neil, M. A. El-Sayed, *Nano Lett.* **2014**, *14*, 743.
- [31] M. Nazemi, S. R. Panikkanvalappil, M. A. El-Sayed, *Nano Energy* **2018**, *49*, 316.
- [32] Y. Guo, J. Tang, Z. Wang, Y. Sugahara, Y. Yamauchi, *Small* **2018**, *14*, 1802442.
- [33] W. Zhu, Z. Chen, Y. Pan, R. Dai, Y. Wu, Z. Zhuang, D. Wang, Q. Peng, C. Chen, Y. Li, *Adv. Mater.* **2019**, *31*, 1800426.
- [34] X. Wang, L. Yu, B. Y. Guan, S. Song, X. W. Lou, *Adv. Mater.* **2018**, *30*, 1801211.
- [35] C. J. M. van der Ham, M. T. M. Koper, D. G. H. Hetterscheid, *Chem. Soc. Rev.* **2014**, *43*, 5183.
- [36] X. Cui, C. Tang, Q. Zhang, *Adv. Energy Mater.* **2018**, *8*, 1800369.
- [37] Y. Abghoui, E. Skúlason, *Catal. Today* **2017**, *286*, 78.
- [38] Y. Abghoui, E. Skúlason, *Catal. Today* **2017**, *286*, 69.
- [39] Y. Abghoui, A. L. Garden, J. G. Howalt, T. Vegge, E. Skúlason, *ACS Catal.* **2015**, *6*, 635.
- [40] Y. Abghoui, E. Skúlason, *J. Phys. Chem. C* **2017**, *121*, 6141.
- [41] C. Ling, Y. Zhang, Q. Li, X. Bai, L. Shi, J. Wang, *J. Am. Chem. Soc.* **2019**, *141*, 18264.
- [42] S. Chen, S. Perathoner, C. Ampelli, C. Mebrahtu, D. Su, G. Centi, *ACS Sustainable Chem. Eng.* **2017**, *5*, 7393.

- [43] Y. Wan, J. Xu, R. Lv, *Mater. Today* **2019**, *27*, 69.
- [44] Y.-C. Hao, Y. Guo, L.-W. Chen, M. Shu, X.-Y. Wang, T.-A. Bu, W.-Y. Gao, N. Zhang, X. Su, X. Feng, J.-W. Zhou, B. Wang, C.-W. Hu, A.-X. Yin, R. Si, Y.-W. Zhang, C.-H. Yan, *Nat. Catal.* **2019**, *2*, 448.
- [45] F. Zhang, Y. Wei, X. Wu, H. Jiang, W. Wang, H. Li, *J. Am. Chem. Soc.* **2014**, *136*, 13963.
- [46] Y. Xia, T. Zhao, X. Zhu, Y. Zhao, H. He, C. T. Hung, X. Zhang, Y. Chen, X. Tang, J. Wang, W. Li, D. Zhao, *Nat. Commun.* **2021**, *12*, 2973.
- [47] H. Wu, G. Zheng, N. Liu, T. J. Carney, Y. Yang, Y. Cui, *Nano Lett.* **2012**, *12*, 904.
- [48] Z. Mao, H. Wang, D. Chao, R. Wang, B. He, Y. Gong, H. J. Fan, *Small* **2020**, *16*, 2001950.
- [49] T. Li, B. Xue, B. Wang, G. Guo, D. Han, Y. Yan, A. Dong, *J. Am. Chem. Soc.* **2017**, *139*, 12133.
- [50] G. Zheng, Y. Yang, J. J. Cha, S. S. Hong, Y. Cui, *Nano Lett.* **2011**, *11*, 4462.
- [51] Q. Sun, N. Wang, J. Yu, J. C. Yu, *Adv. Mater.* **2018**, *30*, 1804368.
- [52] O. Noonan, H. Zhang, H. Song, C. Xu, X. Huang, C. Yu, *J. Mater. Chem. A* **2016**, *4*, 9063.
- [53] R. Fei, H. Wang, Q. Wang, R. Qiu, S. Tang, R. Wang, B. He, Y. Gong, H. J. Fan, *Adv. Energy Mater.* **2020**, *10*, 2002741.
- [54] C. C. Huang, W. Huang, C. S. Yeh, *Biomaterials* **2011**, *32*, 556.
- [55] Z. Li, X. Lai, H. Wang, D. Mao, C. Xing, D. Wang, *J. Phys. Chem. C* **2009**, *113*, 2792.
- [56] X. Lai, J. Li, B. A. Korgel, Z. Dong, Z. Li, F. Su, J. Du, D. Wang, *Angew. Chem., Int. Ed.* **2011**, *50*, 2738.
- [57] J. Wang, H. Tang, L. Zhang, H. Ren, R. Yu, Q. Jin, J. Qi, D. Mao, M. Yang, Y. Wang, P. Liu, Y. Zhang, Y. Wen, L. Gu, G. Ma, Z. Su, Z. Tang, H. Zhao, D. Wang, *Nat. Energy* **2016**, *1*, 16050.
- [58] J. Wang, H. Tang, H. Ren, R. Yu, J. Qi, D. Mao, H. Zhao, D. Wang, *Adv. Sci.* **2014**, *1*, 1400011.
- [59] X. Zhao, R. Yu, H. Tang, D. Mao, J. Qi, B. Wang, Y. Zhang, H. Zhao, W. Hu, D. Wang, *Adv. Mater.* **2017**, *29*, 1700550.
- [60] Z. Dong, X. Lai, J. E. Halpert, N. Yang, L. Yi, J. Zhai, D. Wang, Z. Tang, L. Jiang, *Adv. Mater.* **2012**, *24*, 1046.
- [61] L. Wang, J. Wan, Y. Zhao, N. Yang, D. Wang, *J. Am. Chem. Soc.* **2019**, *141*, 2238.
- [62] W. Guo, W. Sun, Y. Wang, *ACS Nano* **2015**, *9*, 11462.
- [63] Y. Wang, L. Yu, X. W. Lou, *Angew. Chem., Int. Ed.* **2016**, *55*, 14668.
- [64] W. Cho, Y. H. Lee, H. J. Lee, M. Oh, *Adv. Mater.* **2011**, *23*, 1720.
- [65] H. B. Lin, H. B. Rong, W. Z. Huang, Y. H. Liao, L. D. Xing, M. Q. Xu, X. P. Li, W. S. Li, *J. Mater. Chem. A* **2014**, *2*, 14189.
- [66] X. W. Lou, L. A. Archer, Z. Yang, *Adv. Mater.* **2008**, *20*, 3987.
- [67] L. Zhou, Z. Zhuang, H. Zhao, M. Lin, D. Zhao, L. Mai, *Adv. Mater.* **2017**, *29*, 1602914.
- [68] X. Wang, J. Feng, Y. Bai, Q. Zhang, Y. Yin, *Chem. Rev.* **2016**, *116*, 10983.
- [69] X.-J. Wu, D. Xu, *J. Am. Chem. Soc.* **2009**, *131*, 2774.
- [70] J. Cui, Y. Wang, A. Postma, J. Hao, L. Hosta-Rigau, F. Caruso, *Adv. Funct. Mater.* **2010**, *20*, 1625.
- [71] B. Wang, J. S. Chen, H. B. Wu, Z. Wang, X. W. Lou, *J. Am. Chem. Soc.* **2011**, *133*, 17146.
- [72] D. H. M. Buchold, C. Feldmann, *Nano Lett.* **2007**, *7*, 3489.
- [73] G. R. Bourret, R. B. Lennox, *J. Am. Chem. Soc.* **2010**, *132*, 6657.
- [74] Y. Ma, R. Wang, H. Wang, J. Key, S. Ji, *RSC Adv.* **2015**, *5*, 9837.
- [75] Y. Han, M. Fuji, D. Shchukin, H. M \ddot{o} hwald, M. Takahashi, *Cryst. Growth Des.* **2009**, *9*, 3771.
- [76] X. Yan, X. Hu, G. Fu, L. Xu, J.-M. Lee, Y. Tang, *Small* **2018**, *14*, 1703940.
- [77] C. Z. Wu, Y. Xie, L. Y. Lei, S. Q. Hu, C. Z. OuYang, *Adv. Mater.* **2006**, *18*, 1727.
- [78] R. K. Rana, Y. Mastai, A. Gedanken, *Adv. Mater.* **2002**, *14*, 1414.
- [79] Y. Cai, H. Pan, X. Xu, Q. Hu, L. Li, R. Tang, *Chem. Mater.* **2007**, *19*, 3081.
- [80] S. Ding, X. Liu, Y. Shi, Y. Liu, T. Zhou, Z. Guo, J. Hu, *ACS Appl. Mater. Interfaces* **2018**, *10*, 17911.
- [81] A. Li, W. Zhu, C. Li, T. Wang, J. Gong, *Chem. Soc. Rev.* **2019**, *48*, 1874.
- [82] Y. Zhang, Y. Su, Y. Wang, J. He, G. L. McPherson, V. T. John, *RSC Adv.* **2017**, *7*, 39049.
- [83] Y. J. Hong, M. Y. Son, Y. C. Kang, *Adv. Mater.* **2013**, *25*, 2279.
- [84] H. G. Yang, H. C. Zeng, *J. Phys. Chem. B* **2004**, *108*, 3492.
- [85] L. Zhou, J. Zhang, Y. Wu, W. Wang, H. Ming, Q. Sun, L. Wang, J. Ming, H. N. Alshareef, *Adv. Energy Mater.* **2019**, *9*, 1902194.
- [86] D. T. Nguyen, K.-S. Kim, *Chem. Eng. J.* **2016**, *286*, 266.
- [87] S. Zhang, H. Liu, P. Liu, Z. Yang, X. Feng, F. Huo, X. Lu, *Nanoscale* **2015**, *7*, 9411.
- [88] D. Zhang, W. Sun, Y. Zhang, Y. Dou, Y. Jiang, S. X. Dou, *Adv. Funct. Mater.* **2016**, *26*, 7479.
- [89] B. Mao, D. Guo, J. Qin, T. Meng, X. Wang, M. Cao, *Angew. Chem., Int. Ed.* **2018**, *57*, 446.
- [90] S. Kandambeth, V. Venkatesh, D. B. Shinde, S. Kumari, A. Halder, S. Verma, R. Banerjee, *Nat. Commun.* **2015**, *6*, 6786.
- [91] Y. Y. Liu, X. C. Li, S. Wang, T. Cheng, H. Yang, C. Liu, Y. Gong, W. Y. Lai, W. Huang, *Nat. Commun.* **2020**, *11*, 5561.
- [92] Y. Yin, R. M. Rioux, C. K. Erdonmez, S. Hughes, G. A. Somorjai, A. P. Alivisatos, *Science* **2004**, *304*, 711.
- [93] J. G. Railsback, A. C. Johnston-Peck, J. Wang, J. B. Tracy, *ACS Nano* **2010**, *4*, 1913.
- [94] H. Wang, S. Zhuo, Y. Liang, X. Han, B. Zhang, *Angew. Chem., Int. Ed.* **2016**, *55*, 9055.
- [95] Y. Sun, X. Zuo, S. K. R. S. Sankaranarayanan, S. Peng, B. Narayanan, G. Kamath, *Science* **2017**, *356*, 302.
- [96] H. Tianou, W. Wang, X. Yang, Z. Cao, Q. Kuang, Z. Wang, Z. Shan, M. Jin, Y. Yin, *Nat. Commun.* **2017**, *8*, 1261.
- [97] Y. Hu, J. Ge, Y. Sun, T. Zhang, Y. Yin, *Nano Lett.* **2007**, *7*, 1832.
- [98] Q. Zhang, T. Zhang, J. Ge, Y. Yin, *Nano Lett.* **2008**, *8*, 2867.
- [99] M. Hu, S. Furukawa, R. Ohtani, H. Sukegawa, Y. Nemoto, J. Reboul, S. Kitagawa, Y. Yamauchi, *Angew. Chem., Int. Ed.* **2012**, *51*, 984.
- [100] J. H. Pan, Y. Bai, Q. Wang, *Langmuir* **2015**, *31*, 4566.
- [101] N. Yang, F. Pang, J. Ge, *J. Mater. Chem. A* **2015**, *3*, 1133.
- [102] M. Hu, A. A. Belik, M. Imura, Y. Yamauchi, *J. Am. Chem. Soc.* **2013**, *135*, 384.
- [103] D.-S. Bin, Z.-X. Chi, Y. Li, K. Zhang, X. Yang, Y.-G. Sun, J.-Y. Piao, A.-M. Cao, L.-J. Wan, *J. Am. Chem. Soc.* **2017**, *139*, 13492.
- [104] W. Liu, J. Huang, Q. Yang, S. Wang, X. Sun, W. Zhang, J. Liu, F. Huo, *Angew. Chem., Int. Ed.* **2017**, *56*, 5512.
- [105] Y. Sun, B. T. Mayers, Y. Xia, *Nano Lett.* **2002**, *2*, 481.
- [106] Y. Sun, Y. Xia, *Science* **2002**, *298*, 2176.
- [107] C. Peng, W. Yang, E. Wu, Y. Ma, Y. Zheng, Y. Nie, H. Zhang, J. Xu, *J. Alloys Compd.* **2017**, *698*, 250.
- [108] Z. Li, Q. Pei, Y. Yu, Z. Jing, J. Wang, T. He, *ChemCatChem* **2020**, *12*, 4257.
- [109] S. Thota, S. Chen, J. Zhao, *Chem. Commun.* **2016**, *52*, 5593.
- [110] S. Kang, Y.-G. Gil, D.-H. Min, H. Jang, *ACS Nano* **2020**, *14*, 4383.
- [111] B. Cai, D. Wen, W. Liu, A.-K. Herrmann, A. Benad, A. Eychmüller, *Angew. Chem., Int. Ed.* **2015**, *54*, 13101.
- [112] Q. Wang, F. Chen, Q. Tang, L. Guo, T. Jin, B. Pan, J. Wang, Z. Li, B. Kou, W. Bian, *Nano Res.* **2021**, *14*, 2268.
- [113] M. A. Mahmoud, M. A. El-Sayed, *Nano Lett.* **2011**, *11*, 946.
- [114] M. Zhao, Z. Lyu, M. Xie, Z. D. Hood, Z. Cao, M. Chi, Y. Xia, *Small Methods* **2020**, *4*, 1900843.
- [115] M. H. Oh, T. Yu, S.-H. Yu, B. Lim, K.-T. Ko, M.-G. Willinger, D.-H. Seo, B. H. Kim, M. G. Cho, J.-H. Park, K. Kang, Y.-E. Sung, N. Pinna, T. Hyeon, *Science* **2013**, *340*, 964.
- [116] B. Qiao, T. Yang, S. Shi, N. Jia, Y. Chen, X. Chen, Z. An, P. Chen, *Small* **2021**, *17*, 2006534.
- [117] Z. Gao, H. Ye, Q. Wang, M. J. Kim, D. Tang, Z. Xi, Z. Wei, S. Shao, X. Xia, *ACS Nano* **2020**, *14*, 791.

- [118] F. Lyu, Y. Bai, Z. Li, W. Xu, Q. Wang, J. Mao, L. Wang, X. Zhang, Y. Yin, *Adv. Funct. Mater.* **2017**, *27*, 1702324.
- [119] H. Wang, H. Chen, B. Ni, K. Wang, T. He, Y. Wu, X. Wang, *ACS Appl. Mater. Interfaces* **2017**, *9*, 26897.
- [120] S. Xiong, H. C. Zeng, *Angew. Chem., Int. Ed.* **2012**, *51*, 949.
- [121] L. Shen, L. Yu, H. B. Wu, X.-Y. Yu, X. Zhang, X. W. Lou, *Nat. Commun.* **2015**, *6*, 6694.
- [122] H. C. Zeng, *J. Mater. Chem.* **2011**, *21*, 7511.
- [123] P. Liu, H. Zhang, H. Liu, Y. Wang, X. Yao, G. Zhu, S. Zhang, H. Zhao, *J. Am. Chem. Soc.* **2011**, *133*, 19032.
- [124] H. Zhang, O. Noonan, X. Huang, Y. Yang, C. Xu, L. Zhou, C. Yu, *ACS Nano* **2016**, *10*, 4579.
- [125] G. Prieto, H. Tüysüz, N. Duyckaerts, J. Knossalla, G.-H. Wang, F. Schüth, *Chem. Rev.* **2016**, *116*, 14056.
- [126] C. Dai, X. Tian, Y. Nie, C. Tian, C. Yang, Z. Zhou, Y. Li, X. Gao, *Chem. Eng. J.* **2017**, *321*, 105.
- [127] N. Wang, G. Cheng, L. Guo, B. Tan, S. Jin, *Adv. Funct. Mater.* **2019**, *29*, 1904781.
- [128] R. Zhang, H. Guo, L. Yang, Y. Wang, Z. Niu, H. Huang, H. Chen, L. Xia, T. Li, X. Shi, X. Sun, B. Li, Q. Liu, *ChemElectroChem* **2019**, *6*, 1014.
- [129] Z. Xing, W. Kong, T. Wu, H. Xie, T. Wang, Y. Luo, X. Shi, A. M. Asiri, Y. Zhang, X. Sun, *ACS Sustainable Chem. Eng.* **2019**, *7*, 12692.
- [130] J. Wang, Y. Ren, M. Chen, G. Cao, Z. Chen, P. Wang, *J. Alloys Compd.* **2020**, *830*, 154668.
- [131] Y. Zhang, W. Qiu, Y. Ma, Y. Luo, Z. Tian, G. Cui, F. Xie, L. Chen, T. Li, X. Sun, *ACS Catal.* **2018**, *8*, 8540.
- [132] Y. Shao, X. Xiao, Y.-P. Zhu, T.-Y. Ma, *Angew. Chem., Int. Ed.* **2019**, *58*, 14599.
- [133] Y. Guo, Q. Yang, D. Wang, H. Li, Z. Huang, X. Li, Y. Zhao, B. Dong, C. Zhi, *Energy Environ. Sci.* **2020**, *13*, 2888.
- [134] J.-L. Ma, D. Bao, M.-M. Shi, J.-M. Yan, X.-B. Zhang, *Chem* **2017**, *2*, 525.
- [135] J.-T. Ren, L. Chen, H.-Y. Wang, Z.-Y. Yuan, *Chem. Eng. J.* **2021**, *418*, 129447.
- [136] J.-T. Ren, L. Chen, Y. Liu, Z.-Y. Yuan, *J. Mater. Chem. A* **2021**, *9*, 11370.
- [137] U. K. Ghorai, S. Paul, B. Ghorai, A. Adalder, S. Kapse, R. Thapa, A. Nagendra, A. Gain, *ACS Nano* **2021**, *15*, 5230.
- [138] M. Nazemi, M. A. El-Sayed, *J. Phys. Chem. Lett.* **2018**, *9*, 5160.
- [139] S. Cuenot, C. Fréty, S. Demoustier-Champagne, B. Nysten, *Phys. Rev. B* **2004**, *69*, 165410.
- [140] M. Rycenga, C. M. Cobley, J. Zeng, W. Li, C. H. Moran, Q. Zhang, D. Qin, Y. Xia, *Chem. Rev.* **2011**, *111*, 3669.
- [141] C. Huang, T. Ouyang, Y. Zou, N. Li, Z. Q. Liu, *J. Mater. Chem. A* **2018**, *6*, 7420.
- [142] Q. Lu, J. Yu, X. Zou, K. Liao, P. Tan, W. Zhou, M. Ni, Z. Shao, *Adv. Funct. Mater.* **2019**, *29*, 1904481.
- [143] J.-T. Ren, C.-Y. Wan, T.-Y. Pei, X.-W. Lv, Z.-Y. Yuan, *Appl. Catal., B* **2020**, *266*, 118633.
- [144] F. Xu, L. Zhang, X. Ding, M. Cong, Y. Jin, Y. Gao, L. Chen, *Chem. Commun.* **2019**, *55*, 14111.
- [145] L. Cong, Z. Yu, F. Liu, W. Huang, *Catal. Sci. Technol.* **2019**, *9*, 1208.
- [146] H. Li, T.-T. Li, J. Qian, Y. Mei, Y.-Q. Zheng, *Int. J. Hydrogen Energy* **2020**, *45*, 14640.
- [147] G.-R. Xu, M. Batmunkh, S. Donne, H. Jin, J.-X. Jiang, Y. Chen, T. Ma, *J. Mater. Chem. A* **2019**, *7*, 25433.
- [148] J. Zhang, Y. Tian, T. Zhang, Z. Li, X. She, Y. Wu, Y. Wang, J. Wu, *ChemCatChem* **2020**, *12*, 2760.
- [149] Y.-T. Liu, D. Li, J. Yu, B. Ding, *Angew. Chem., Int. Ed.* **2019**, *58*, 16439.
- [150] J. Lin, P. Wang, H. Wang, C. Li, X. Si, J. Qi, J. Cao, Z. Zhong, W. Fei, J. Feng, *Adv. Sci.* **2019**, *6*, 1900246.
- [151] Z. Li, M. Song, W. Zhu, W. Zhuang, X. Du, L. Tian, *Coord. Chem. Rev.* **2021**, *439*, 213946.
- [152] H. Shan, Y. Yu, R. Zhang, R. Cheng, D. Zhang, Y. Luo, X. Wang, B. Li, S. Zu, F. Lin, Z. Liu, K. Chang, Z. Fang, *Mater. Today* **2019**, *24*, 10.
- [153] Y. Li, W. Zheng, H. Zhang, H. Wang, H. Cai, Y. Zhang, Z. Yang, *Nano Energy* **2020**, *70*, 104540.
- [154] C. Niu, X. Liu, J. Meng, L. Xu, M. Yan, X. Wang, G. Zhang, Z. Liu, X. Xu, L. Mai, *Nano Energy* **2016**, *27*, 147.
- [155] M. Huang, Y. Chu, B. Xi, N. Shi, B. Duan, C. Zhang, W. Chen, J. Feng, S. Xiong, *Small* **2020**, *16*, 2004054.
- [156] G. Zhao, K. Rui, S. X. Dou, W. Sun, *Adv. Funct. Mater.* **2018**, *28*, 1803291.
- [157] S. Wang, Y. Wang, S.-Q. Zang, X. W. Lou, *Small Methods* **2020**, *4*, 1900586.
- [158] Z. Liang, W. Zhou, S. Gao, R. Zhao, H. Zhang, Y. Tang, J. Cheng, T. Qiu, B. Zhu, C. Qu, W. Guo, Q. Wang, R. Zou, *Small* **2020**, *16*, 1905075.
- [159] S.-Q. Liu, H.-R. Wen, G. Ying, Y.-W. Zhu, X.-Z. Fu, R. Sun, C.-P. Wong, *Nano Energy* **2018**, *44*, 7.
- [160] L. Chen, C. Zhang, Y. Li, C.-R. Chang, C. He, Q. Lu, Y. Yu, P. Duan, Z. Zhang, R. Luque, *ACS Catal.* **2021**, *11*, 10988.
- [161] X. Wu, Z. Wang, Y. Han, D. Zhang, M. Wang, H. Li, H. Zhao, Y. Pan, J. Lai, L. Wang, *J. Mater. Chem. A* **2020**, *8*, 543.
- [162] M. Arif, G. Yasin, L. Luo, W. Ye, M. A. Mushtaq, X. Fang, X. Xiang, S. Ji, D. Yan, *Appl. Catal., B* **2020**, *265*, 118559.
- [163] M. Yuan, Y. Bai, J. Zhang, T. Zhao, S. Li, H. He, Z. Liu, Z. Wang, G. Zhang, *J. Mater. Chem. A* **2020**, *8*, 26066.
- [164] J. Lv, S. Wu, Z. Tian, Y. Ye, J. Liu, C. Liang, *J. Mater. Chem. A* **2019**, *7*, 12627.
- [165] S. Luo, X. Li, W. Gao, H. Zhang, M. Luo, *Sustainable Energy Fuels* **2020**, *4*, 164.
- [166] S. Luo, X. Li, B. Zhang, Z. Luo, M. Luo, *ACS Appl. Mater. Interfaces* **2019**, *11*, 26891.
- [167] S. Liu, Y. Xu, S. Jiao, W. Tian, T. Zhou, Z. Wang, X. Li, L. Wang, H. Wang, *J. Mater. Chem. A* **2021**, *9*, 8372.
- [168] T. Wu, X. Zhu, Z. Xing, S. Mou, C. Li, Y. Qiao, Q. Liu, Y. Luo, X. Shi, Y. Zhang, X. Sun, *Angew. Chem., Int. Ed.* **2019**, *58*, 18449.
- [169] L. Zhang, M. Cong, X. Ding, Y. Jin, F. Xu, Y. Wang, L. Chen, L. Zhang, *Angew. Chem., Int. Ed.* **2020**, *59*, 10888.
- [170] Y. Liu, Y. Su, X. Quan, X. Fan, S. Chen, H. Yu, H. Zhao, Y. Zhang, J. Zhao, *ACS Catal.* **2018**, *8*, 1186.
- [171] L. Xia, X. Wu, Y. Wang, Z. Niu, Q. Liu, T. Li, X. Shi, A. M. Asiri, X. Sun, *Small Methods* **2019**, *3*, 1800251.
- [172] L.-P. Yuan, Z.-Y. Wu, W.-J. Jiang, T. Tang, S. Niu, J.-S. Hu, *Nano Res.* **2020**, *13*, 1376.
- [173] Z. Wu, Y. Zhao, W. Jin, B. Jia, J. Wang, T. Ma, *Adv. Funct. Mater.* **2021**, *31*, 2009070.
- [174] X.-W. Lv, X. Liu, L. Gao, Y. Liu, Z.-Y. Yuan, *J. Mater. Chem. A* **2021**, *9*, 4026.
- [175] N. Cao, Z. Chen, K. Zang, J. Xu, J. Zhong, J. Luo, X. Xu, G. Zheng, *Nat. Commun.* **2019**, *10*, 2877.
- [176] W. Ye, Y. Yang, M. Arif, S. Yang, X. Fang, M. A. Mushtaq, X. Chen, D. Yan, *ACS Sustainable Chem. Eng.* **2020**, *8*, 15946.
- [177] Y. Deng, Z. Xiao, Z. Wang, J. Lai, X. Liu, D. Zhang, Y. Han, S. Li, W. Sun, L. Wang, *Appl. Catal., B* **2021**, *291*, 120047.
- [178] L. Zeng, X. Li, S. Chen, J. Wen, W. Huang, A. Chen, *J. Mater. Chem. A* **2020**, *8*, 7339.
- [179] D. Lee, X. Gao, L. Sun, Y. Jee, J. Poplawsky, T. O. Farmer, L. Fan, E.-J. Guo, Q. Lu, W. T. Heller, Y. Choi, D. Haskel, M. R. Fitzsimmons, M. F. Chisholm, K. Huang, B. Yildiz, H. N. Lee, *Nat. Commun.* **2020**, *11*, 1371.
- [180] L. Zeng, S. Chen, J. Zalm, X. Li, A. Chen, *Chem. Commun.* **2019**, *55*, 7386.
- [181] H. Y. Jin, L. Q. Li, X. Liu, C. Tang, W. J. Xu, S. M. Chen, L. Song, Y. Zheng, S. Z. Qiao, *Adv. Mater.* **2019**, *31*, 1902709.

- [182] Y. Wang, R. Gan, Z. Ai, H. Liu, C. Wei, Y. Song, M. Dirican, X. Zhang, C. Ma, J. Shi, *Carbon* **2021**, *181*, 87.
- [183] A. Kumar, M. Kumar, V. Navakoteswara Rao, M. V. Shankar, S. Bhat-tacharya, V. Krishnan, *J. Mater. Chem. A* **2021**, *9*, 17006.
- [184] Y. Wang, Y. Zhang, Z. Liu, C. Xie, S. Feng, D. Liu, M. Shao, S. Wang, *Angew. Chem., Int. Ed.* **2017**, *56*, 5867.
- [185] Z. Wang, J. Shen, W. Fu, J. Liao, J. Dong, P. Zhuang, Z. Cao, Z. Ye, J. Shi, M. Ye, *Inorg. Chem. Front.* **2020**, *7*, 3609.
- [186] F. Lai, J. Feng, X. Ye, W. Zong, G. He, C. Yang, W. Wang, Y.-E. Miao, B. Pan, W. Yan, T. Liu, I. P. Parkin, *J. Mater. Chem. A* **2020**, *8*, 1652.
- [187] X. Yang, F. Ling, J. Su, X. Zi, H. Zhang, H. Zhang, J. Li, M. Zhou, Y. Wang, *Appl. Catal., B* **2020**, *264*, 118477.
- [188] M. Ma, X. Han, H. Li, X. Zhang, Z. Zheng, L. Zhou, J. Zheng, Z. Xie, Q. Kuang, L. Zheng, *Appl. Catal., B* **2020**, *265*, 118568.
- [189] S. Ji, Y. Chen, X. Wang, Z. Zhang, D. Wang, Y. Li, *Chem. Rev.* **2020**, *120*, 11900.
- [190] H. Hu, W. Guan, Y. Xu, X. Wang, L. Wu, M. Chen, Q. Zhong, Y. Xu, Y. Li, T.-K. Sham, X. Zhang, L. Wang, M. Cao, Q. Zhang, *ACS Nano* **2021**, *15*, 13129.
- [191] Y.-C. Hao, L.-W. Chen, J. Li, Y. Guo, X. Su, M. Shu, Q. Zhang, W.-Y. Gao, S. Li, Z.-L. Yu, L. Gu, X. Feng, A.-X. Yin, R. Si, Y.-W. Zhang, B. Wang, C.-H. Yan, *Nat. Commun.* **2021**, *12*, 2682.
- [192] S. Ji, Y. Qu, T. Wang, Y. Chen, G. Wang, X. Li, J. Dong, Q. Y. Chen, W. Zhang, Z. Zhang, S. Liang, R. Yu, Y. Wang, D. Wang, Y. Li, *Angew. Chem., Int. Ed.* **2020**, *59*, 10651.
- [193] P. Li, M. Wang, X. Duan, L. Zheng, X. Cheng, Y. Zhang, Y. Kuang, Y. Li, Q. Ma, Z. Feng, W. Liu, X. Sun, *Nat. Commun.* **2019**, *10*, 1711.
- [194] C. Hu, E. Song, M. Wang, W. Chen, F. Huang, Z. Feng, J. Liu, J. Wang, *Adv. Sci.* **2021**, *8*, 2001881.
- [195] W. Zang, T. Yang, H. Zou, S. Xi, H. Zhang, X. Liu, Z. Kou, Y. Du, Y. P. Feng, L. Shen, L. Duan, J. Wang, S. J. Pennycook, *ACS Catal.* **2019**, *9*, 10166.
- [196] E. Tiburcio, R. Greco, M. Mon, J. Ballesteros-Soberanas, J. Ferrando-Soria, M. Lopez-Haro, J. C. Hernandez-Garrido, J. Oliver-Meseguer, C. Marini, M. Boronat, D. Armentano, A. Leyva-Perez, E. Pardo, *J. Am. Chem. Soc.* **2021**, *143*, 2581.
- [197] Y. Wang, X. Cui, J. Zhao, G. Jia, L. Gu, Q. Zhang, L. Meng, Z. Shi, L. Zheng, C. Wang, Z. Zhang, W. Zheng, *ACS Catal.* **2019**, *9*, 336.
- [198] Y. Ma, W. Zang, Z. Kou, S. J. Pennycook, J. Wang, Y. Ma, L. Mao, X. Li, T. Yang, Y. Feng, H. Zou, L. Duan, L. Shen, *Adv. Mater.* **2020**, *32*, 2002177.
- [199] X. Wang, S. Qiu, J. Feng, Y. Tong, F. Zhou, Q. Li, L. Song, S. Chen, K.-H. Wu, P. Su, S. Ye, F. Hou, S. X. Dou, H. K. Liu, G. Q. Lu, C. Sun, J. Liu, J. Liang, *Adv. Mater.* **2020**, *32*, 2004382.
- [200] X. Guo, J. Gu, S. Lin, S. Zhang, Z. Chen, S. Huang, *J. Am. Chem. Soc.* **2020**, *142*, 5709.
- [201] R. D. L. Smith, M. S. Prevot, R. D. Fagan, Z. P. Zhang, P. A. Sedach, M. K. J. Siu, S. Trudel, C. P. Berlinguette, *Science* **2013**, *340*, 60.
- [202] P. D. Tran, Thu V. Tran, M. Orio, S. Torelli, Q. D. Truong, K. Nayuki, Y. Sasaki, S. Y. Chiam, R. Yi, I. Honma, J. Barber, V. Artero, *Nat. Mater.* **2016**, *15*, 640.
- [203] C. Lv, C. Yan, G. Chen, Y. Ding, J. Sun, Y. Zhou, G. Yu, *Angew. Chem., Int. Ed.* **2018**, *57*, 6073.
- [204] H. Li, C. Tsai, A. L. Koh, L. Cai, A. W. Contryman, A. H. Fragapane, J. Zhao, H. S. Han, H. C. Manoharan, F. Abild-Pedersen, J. K. Nørskov, X. Zheng, *Nat. Mater.* **2016**, *15*, 48.
- [205] H. Wang, S. Xu, C. Tsai, Y. Li, C. Liu, J. Zhao, Y. Liu, H. Yuan, F. Abild-Pedersen, F. B. Prinz, J. K. Nørskov, Y. Cui, *Science* **2016**, *354*, 1031.
- [206] Z. Ma, J. Chen, T. Thersleff, A. Slabon, D. Luo, R. Dronskowski, *Nanoscale* **2020**, *12*, 19276.
- [207] M. Nazemi, L. Soule, M. Liu, M. A. El-Sayed, *J. Electrochem. Soc.* **2020**, *167*, 054511.
- [208] L. Zeng, X. Li, S. Chen, J. Wen, F. Rahmati, J. van der Zalm, A. Chen, *Nanoscale* **2020**, *12*, 6029.
- [209] X. Xu, Y. Wang, X. Chen, X. Qian, Z. Liang, H. Cui, J. Tian, M. Shao, *EcoMat* **2021**, *3*, e12122.
- [210] T. Wu, P. Li, H. Wang, R. Zhao, Q. Zhou, W. Kong, M. Liu, Y. Zhang, X. Sun, F. Gong, *Chem. Commun.* **2019**, *55*, 2684.
- [211] J. X. Zhao, B. Wang, Q. Zhou, H. B. Wang, X. H. Li, H. Y. Chen, Q. Wei, D. Wu, Y. L. Luo, J. M. You, F. Gong, X. P. Sun, *Chem. Commun.* **2019**, *55*, 4997.
- [212] W. Guo, Z. Liang, J. Zhao, B. Zhu, K. Cai, R. Zou, Q. Xu, *Small Meth-ods* **2018**, *2*, 1800204.
- [213] C. Wang, L.-L. Gu, S.-Y. Qiu, J. Gao, Y.-C. Zhang, K.-X. Wang, J.-J. Zou, P.-J. Zuo, X.-D. Zhu, *Appl. Catal., B* **2021**, *297*, 120452.



Cong Xue obtained his B.S. degree from the Yancheng Institute of Technology (China) in 2018. He is currently a Master's degree candidate under the guidance of Prof. Wenjing Liu at the Institute of Advanced Materials, Nanjing Tech University. His research interest is the synthesis and design of hollow structural materials for energy conversion applications such as electrochemical nitrogen and nitrate reduction.



Wenjing Liu received her Ph.D. degree in Chemistry from the Department of Life Sciences and Chemistry, Jacobs University, Bremen, Germany in 2015. After postdoctoral research at the Nanjing Normal University in 2018, she is currently an Associate Professor at the Nanjing Tech University. Her research interests focus on the application of boron-cluster-based nanomaterials and polyoxometalate-based materials in energy storage and conversion.



Fengwei Huo obtained his B.S. and M.S. degrees from the Jilin University (China) in 1999 and 2002, respectively. He completed his Ph.D. at the Northwestern University (US) in 2009. Then, he joined the Nanyang Technological University as an Assistant Professor. In 2014, he moved to the Institute of Advanced Materials, Nanjing Tech University as a Full Professor. From 2017, he has served as an Associate Editor of ACS Applied Materials & Interfaces. His current research involves functional nanomaterials, metal–organic framework materials, and flexible electronics.